JTSES
Journal of Thermal and Sustainable Energy Systems
https://jtses.com/index.php/home/index

Self-Sensing AlCrFeNiSi/Ti_3AlC_2 Nanolaminates Enable Innovative Temperature-Compensated Monitoring of Molten-Chloride Damage

Sathish Kumar Manickam [1]*, Vasudhevan Dhevarajan [2], Vijaya Subramanian [3], Parthiban Alagesan [4]

[1] Department of Mechanical Engineering, Paavai College of Engineering, Namakkal – 637018, Tamil Nadu, India — Email: sathishskymech@gmail.com

[2] Department of Mechanical Engineering, K. S. Rangasamy College of Technology, Namakkal, Tamil Nadu, India — Email: vasudevan.vi@gmail.com

[3] Department of Electronics and Communication Engineering, Paavai Engineering College, Namakkal – 637018, Tamil Nadu, India — Email: sscetvijaya@gmail.com

[4] Department of Mechanical Engineering, Vels Institute of Science, Technology & Advanced Studies (VISTAS), Pallavaram, Chennai – 600117, Tamil Nadu, India — Email: parthibana83@gmail.com

Corresponding Author*: Sathish Kumar Manickam — Email: sathishskymech@gmail.com

ABSTRACT

Molten chloride salts support high-temperature heat transfer and thermal-energy storage, but aggressive dissolution and unstable protective scales restrict structural-alloy durability. Multifunctional coatings integrating corrosion resistance with damage detection are therefore required for reliable molten-salt components. Existing inorganic coatings do not provide depth-resolved, temperature-compensated electrical warning before substrate breakthrough. This investigation establishes an innovative AlCrFeNiSi/Ti_3AlC_2 nanolaminate that combines chloride protection with embedded MAX-phase damage sentinels. Three modulation-period architectures were evaluated using composition-derived descriptors, geometrical calculations, four-terminal resistance sensing, temperature correction, electrochemical impedance spectroscopy, dissolved-metal monitoring, and event-triggered microscopy. A 3.50 µm coating containing 0.50 µm Ti_3AlC_2 produced a 14.29% full-coating MAX fraction. Interface density decreased from 13.33 to 3.33 μm^{-1} across the L150–L600 architectures while phase proportions remained constant, isolating modulation-period effects. Changing H21S8 to H21S5 increased the Al/Si ratio by 60%, whereas configurational entropy decreased by only 2.6%. Idealized conductive-area loss doubled normalized resistance at 50% remaining area and increased it tenfold at 10%, demonstrating nonlinear damage sensitivity. The architecture provides a quantitative platform for separating thermal, chemical, and mechanical resistance changes. It supports condition-based monitoring of thermal-storage and reactor components exposed to chloride melts. Future research validates warning lead, interfacial stability, and sensor durability through long-duration exposures and depth-correlated microscopy.

KEYWORDS: AlCrFeNiSi nanolaminates, Ti_3AlC_2 sentinels, Molten-chloride corrosion, Resistance sensing, Interface engineering

INTRODUCTION

Molten chloride salts have attracted sustained interest as heat-transfer and thermal-energy-storage media because their thermal stability permits operation well above the temperature ceiling of conventional nitrate salts. $MgCl_2$–KCl–NaCl has accordingly been positioned as a candidate for next-generation high-temperature systems, although its engineering value depends directly on corrosion control (Villada et al., 2021). At the metal–salt interface, corrosion cannot be treated as a simple oxidation problem. First-principles molecular-dynamics calculations combined with electrochemical measurements showed that Fe and Cr dissolution in $MgCl_2$–NaCl was governed by both redox thermodynamics and chloride-mediated transport kinetics (X. Li et al., 2022). Experiments on Ni-based alloys in molten KCl likewise identified preferential Cr dissolution along grain boundaries, demonstrating that nominally corrosion-resistant alloying additions can become selective dissolution pathways in chloride melts (Choi et al., 2024). Salt chemistry further complicated this response: sulfate contamination promoted severe intergranular attack of 316H stainless steel in $MgCl_2$–KCl–NaCl (Ai et al., 2024). These observations made purification an experimental variable rather than a preparatory detail. Continuous electrolytic purification with alternating Mg electrodes suppressed corrosive impurity activity and provided a route toward sustained chloride conditioning (Ding et al., 2021).

High-entropy alloys offered a different route to corrosion control because phase chemistry, local elemental partitioning, and surface-reaction pathways could be manipulated simultaneously. TaTiVWZr and HfTaTiVZr refractory HEAs showed substantially stronger resistance than SS316 during FLiNaK exposure, although selective dissolution remained dependent on local microstructure (Patel et al., 2023a). Composition could not be optimized from elemental richness alone: Al variation within $Al_xCrFeNi_{3-x}$ eutectic HEAs altered passive-film chemistry and phase-specific electrochemical activity in chloride solution (Zhao et al., 2022). A cost-reduced AlCrFeNi eutectic alloy similarly linked corrosion performance to FCC fraction and compact passive-film formation (Wu et al., 2023). Arc-clad CrMnFeCoNi coatings demonstrated that a continuous passive film could protect steel in aqueous chloride, but that environment did not reproduce molten-salt thermochemistry (Wang et al., 2022). Laser-clad $FeCoNiCrAl_{0.6}$ coatings further showed that small electrochemical differences between constituent phases could suppress localized galvanic activity (Yuan et al., 2023). Heat treatment subsequently altered the BCC/FCC morphology and corrosion response of $AlCoCrFeNi_{2.1}$, emphasizing that post-deposition processing remained inseparable from composition (Dong et al., 2025). Under molten Na_2SO_4–NaCl, $AlCoCrFeNi_{2.1}$ coatings also exhibited phase and oxide-scale changes after thermal exposure (Zhang et al., 2023). Extreme high-speed laser cladding and remelting refined the same alloy system and promoted more uniform Al_2O_3 formation during hot corrosion (Zhang et al., 2024). Plasma-sprayed AlCoCrFeNiTi coatings extended HEA coating concepts to vanadate-containing molten salts, but their corrosion chemistry differed markedly from $MgCl_2$-rich media (Odabas et al., 2024). More recently, Cu/Mo partitioning in $AlCrCu_{1-x}Mo_xNi$ coatings was shown to control the development of Cr-rich and Al-rich layers during composite molten-salt attack at 700 °C (Yang et al., 2025). Table 1 summarizes the methodological contrasts most relevant to the present coating and sensing strategy.

Table 1:**studies linking molten-salt corrosion, HEA/MAX-phase protection, salt conditioning, and corrosion sensing.**

Reference/Citation	Objective/Aim	Methodology/Approach	Materials/Parameters Studied	Key Findings/Results	Relevance to Current Study
(Patel et al., 2021)	Benchmark refractory HEAs in CSP chloride melts	Polarization, immersion, surface characterization	TaTiVWZr, HfTaTiVZr; NaCl–KCl–$MgCl_2$; 450–650 °C	△ TaTiVWZr outperformed SS304 under identical chloride exposure	Benchmarks HEA resistance in $MgCl_2$-based salt
(Patel et al., 2023b)	Resolve dual-phase HEA corrosion mechanisms	Polarization, immersion, SKP, surface analysis	$AlCoCrFeNi_{2.1}$; NaCl–KCl–$MgCl_2$; 450–650 °C	△ EHEA resisted chloride attack better than duplex steel	Links phase contrast with selective dissolution
(Xie et al., 2024)	Suppress chloride–sulfate attack using HEA cladding	Laser cladding, XRD, SEM, hot corrosion	FeCrNiMoAl; chloride–sulfate salt; 600 °C	△ Cr_2O_3/Al_2O_3 bilayer restricted chlorine and sulfur penetration	Supports Al–Cr barrier chemistry under hot salts

Reference/Citation	Objective/Aim	Methodology/Approach	Materials/Parameters Studied	Key Findings/Results	Relevance to Current Study
(Magnus et al., 2021)	Determine Ti_3AlC_2 degradation in molten chloride	SPS, immersion, SEM, XRD, GAXRD	Ti_3AlC_2; LiCl–KCl; 600 °C	▽ Al dissolution triggered delamination and chlorine intercalation	Defines chemical baseline for MAX resistance sensing
(Z. Li et al., 2023)	Lower synthesis temperature for Ti_3AlC_2 coatings	HiPIMS, DCMS comparison, annealing, XRD	Ti–Al–C films; Ti-6Al-4V; 700 °C	△ HiPIMS yielded dense Ti_3AlC_2 after 700 °C annealing	Supports conductive MAX interlayer fabrication
(Zhao & Gomez-Vidal, 2020)	Develop scalable $MgCl_2$ salt purification	Thermal–chemical treatment, impurity quantification	Carnallite, NaCl, Mg; MgOHCl control	▽ MgOHCl approached 0.1 wt% after optimized purification	Controls melt chemistry before coating comparison
(Grégoire et al., 2020)	Resolve impurity-driven alloy attack in ternary chloride	Exposure, microscopy, Raman, thermodynamic analysis	P91, Inconel 600; ternary chloride; 700 °C	▽ Cr depletion accompanied voiding and carbide removal	Provides substrate and impurity corrosion benchmark
(Gong et al., 2022)	Validate affordable alloys in purified CSP chloride	2000 h immersion, SEM–EDX, mass analysis	SS310, Incoloy 800H; ternary chloride; 700 °C	△ Purification sustained alloy attack below 15 μm $year^{-1}$	Sets long-duration application benchmark
(Liu et al., 2022)	Integrate corrosion warning with active protection	Responsive microcontainers, EIS, salt-spray testing	Epoxy, Q235 steel, $CaCO_3$–APhen microcontainers	△ Visual warning developed within two minutes during corrosion	Demonstrates protection–sensing integration
(Takeyama, 2025)	Correct ER monitoring under temperature fluctuations	Improved electrical-resistance sensing, thermal compensation	ER sensor; fluctuating-temperature environment	△ Thermal compensation stabilized high-temporal-resolution ER monitoring	Supports thermal correction of conductive sentinels

Conductive MAX phases added a second functional dimension because they could provide both high-temperature interfaces and electrically interrogated pathways. Their corrosion response, however, depended sharply on chemistry. PVD-derived Cr_2AlC, Ti_2AlC, and Ti_3AlC_2 coatings survived long exposure to oxygen-containing molten Pb through protective oxide formation, whereas V_2AlC was largely consumed under the same conditions (Shi et al., 2022). In solar salt at 600 °C, Cr_2AlC provided stronger protection than Ti_2AlC and Ti_3AlC_2 through a thin protective surface layer, again showing that MAX-phase stability could not be generalized across environments (Azina et al., 2023). Processing also controlled function: filtered-cathodic-vacuum-arc Ti_3AlC_2 coatings required sufficient carbon availability and post-deposition annealing to establish the desired phase, and their electrochemical response varied with deposition condition (H. Li et al., 2022). Beyond barrier materials, smart-coating research increasingly targeted detection before visually apparent failure, but most reported sensing concepts remained associated with polymeric coatings and comparatively mild environments (Xiao et al., 2023). Meanwhile, long-duration tests in purified $MgCl_2$–KCl–NaCl demonstrated that corrosion control could enable lower-cost structural materials, linking laboratory salt conditioning directly to system scalability (Gong et al., 2023).

These findings collectively shifted the design problem from selecting a single corrosion-resistant material toward engineering a coupled material–environment–measurement system. Dense HEA layers could supply chemical and structural resistance, while nanoscale interfaces could interrupt through-thickness transport and redirect crack propagation. A conductive MAX phase could additionally convert local degradation into an electrical observable, provided that chemical drift, thermal resistance changes, and mechanical interruption were separated experimentally. That distinction was essential because high-temperature resistance signals could otherwise reflect temperature rather than damage, while chloride-induced alteration of Ti_3AlC_2 could precede physical fracture. At the same time, meaningful coating comparisons required controlled salt purification because alloy ranking could be overwhelmed by uncontrolled MgOHCl, sulfate, moisture, or redox differences. The resulting experimental framework therefore required composition control, multilayer architecture, salt chemistry, electrochemical response, electrical sensing, and post-exposure microstructural evidence to be interpreted together rather than as independent performance indicators.

Laser cladding, arc or plasma deposition, PVD/HiPIMS processing, immersion testing, electrochemical spectroscopy, and multiscale microscopy dominated the experimental approaches across the selected literature (Zhang et al., 2024). Favorable HEA behavior was repeatedly associated with controlled phase morphology and protective Al- or Cr-containing surface products, whereas selective dissolution remained sensitive to local phase chemistry (Zhao et al., 2022). Composite molten-salt studies further showed that changing Cu/Mo partitioning altered protective-layer development and corrosion pathways (Yang et al., 2025). Salt studies consistently identified impurity conditioning as a controlling process variable rather than a secondary procedural step (Ding et al., 2021). MAX-phase and sensing studies likewise showed that environmental compatibility, fabrication route, and signal interpretation had to be considered jointly (Shi et al., 2022).

The literature therefore moved toward increasingly engineered corrosion-control systems in which alloy chemistry, coating processing, salt purification, and diagnostic monitoring were treated as interacting variables. Chloride-salt engineering already incorporated both mitigation and monitoring concepts at the system level (Villada et al., 2021), while smart-coating research increasingly emphasized detection of subsurface degradation before macroscopic coating failure (Xiao et al., 2023). However, these developments remained distributed across largely separate material and sensing platforms.

Existing studies did not resolve how corrosion protection and electrically depth-resolved damage detection could be coupled within the same high-temperature chloride-resistant coating. HEA investigations covered restricted and mutually different composition ranges, deposition routes, salt chemistries, temperatures, and exposure protocols, which limited direct performance comparison (Patel et al., 2023a). Process-dependent results from laser-clad HEAs further showed that inconsistent fabrication histories altered microstructure and oxide development, complicating transfer between studies (Zhang et al., 2024). MAX-phase investigations established strong environment dependence, but bulk specimens, molten Pb, solar salt, or stand-alone coatings dominated the available validation rather than electrically isolated nanolaminate sentinels in molten chlorides (Shi et al., 2022).

Smart sensing studies largely separated corrosion detection from high-temperature inorganic barrier architectures, leaving thermal compensation and long-duration signal stability insufficiently coupled to microscopic failure verification (Xiao et al., 2023). Salt-conditioning studies demonstrated that impurity control could govern measured corrosion behavior, yet purification, coating architecture, electrical sensing, EIS, dissolved-metal analysis, and damage-depth microscopy were rarely evaluated within one coordinated protocol (Ding et al., 2021). Finally, promising laboratory-scale coating and salt-control strategies still faced scalability constraints because extended exposure, batch-to-batch reproducibility, sensor durability, and independent validation under thermal cycling remained limited or methodologically inconsistent (Gong et al., 2023).

The present study addressed these limitations through an AlCrFeNiSi/Ti_3AlC_2 nanolaminate architecture in which HEA chemistry, Al:Si ratio, modulation period, and deposition bias were controlled systematically, while conductive MAX-phase layers were configured as electrically isolated sensing elements at shallow, intermediate, and near-substrate depths. Four-terminal resistance measurements were combined with specimen-specific temperature compensation and time-multiplexed EIS so that thermal drift, electrical discontinuity, and electrochemical degradation could be separated. Purified and impurity-controlled LiCl–KCl and $MgCl_2$–KCl–NaCl environments were incorporated under both isothermal and thermal-cycling conditions, and resistance events were linked to salt chemistry, metal-ion dissolution, profilometry, FIB–SEM/TEM, XPS, and XRD evidence. Batch-aware statistical analysis and interpretable temporal modelling were incorporated to test whether electrical warning remained transferable across independently deposited specimens rather than being inferred from repeated time points from the same coating.

The objective of the present study is to establish and validate an AlCrFeNiSi/Ti_3AlC_2 self-sensing nanolaminate coating that couples molten-chloride corrosion protection with depth-resolved, temperature-corrected electrical early-damage detection under controlled isothermal and thermal-cycling conditions.

2. MATERIALS AND METHODS

2.1. Experimental design and coating architecture

A staged experimental programme was used to investigate the coupled effects of AlCrFeNiSi high-entropy-alloy composition, HEA/MAX-phase modulation period, substrate bias, molten-chloride chemistry, and embedded electrical sensing. The experimental sequence was divided into HEA-composition screening, MAX-phase thin-film qualification, nanolaminate architecture optimization, electrical-sensor calibration, molten-salt exposure, post-exposure microstructural validation, and statistical integration of the resulting electrochemical and electrical time-series data. Independent deposition batches and independent molten-salt cells were treated as the principal experimental units. Repeated electrical measurements, impedance spectra, microscopy fields, elemental maps, and mechanical measurements acquired from the same specimen were treated as repeated observations or subsamples rather than independent replicates.

Three Al–Cr–Fe–Ni–Si chemistries were examined during the initial composition-screening stage. The nominal compositions were $Al_{21}Cr_{23.67}Fe_{23.67}Ni_{23.67}Si_8$, $Al_{25}Cr_{22.33}Fe_{22.33}Ni_{22.33}Si_8$, and $Al_{21}Cr_{24.67}Fe_{24.67}Ni_{24.67}Si_5$, designated H21S8, H25S8, and H21S5, respectively. The H21S8 composition was centred on the recently investigated $Al_{21}CrFeNiSi_8$ chemistry, whereas the H25S8 and H21S5 variants were included to separate the effects of increased Al availability and reduced Si content. This compositional range was selected because Al enrichment was expected to favour formation of an Al-rich protective surface oxide, whereas excessive Si was expected to increase the likelihood of silicide- and intermetallic-rich phase formation [1].

Ti_3AlC_2 was used as the principal conductive MAX phase. The material was selected because its layered structure, electrical conductivity, and previously established interaction with molten LiCl–KCl allowed it to function simultaneously as a structural interlayer and as a chemically responsive electrical sentinel [2]. V_2AlC was included as a secondary exploratory MAX-phase comparator. An Al_2O_3-interlayer architecture was used as a nonconductive multilayer control so that improvements arising from interface density could be distinguished from those associated specifically with conductive MAX-phase interlayers.

Inconel 625 was used as the principal Ni-based substrate, while AISI 316L stainless steel was used as the Fe-based comparison substrate. General corrosion coupons were prepared with nominal dimensions of 20 × 15 × 2–3 mm. Instrumented sensing coupons were prepared with nominal dimensions of 30 × 10 × 2–3 mm so that the electrical contact pads and lead junctions could be positioned outside the molten-salt wet zone.

A nominal total coating thickness of approximately 3.5 μm was maintained for the principal architecture comparison. A graded HEA base region of approximately 200 nm and an outer HEA cap of approximately 300 nm were incorporated into the multilayer specimens. The central multilayer region was maintained at approximately 3.0 μm. Three modulation periods were investigated while the total coating thickness and approximate MAX-phase fraction were maintained as closely as practicable. The fine architecture consisted of approximately 125 nm HEA/25 nm MAX bilayers repeated 20 times, the intermediate architecture consisted of approximately 250 nm HEA/50 nm MAX bilayers repeated 10 times, and the coarse architecture consisted of approximately 500 nm HEA/100 nm MAX bilayers repeated five times.

The complete material architecture and experimental fabrication sequence were represented schematically in Fig. 1.

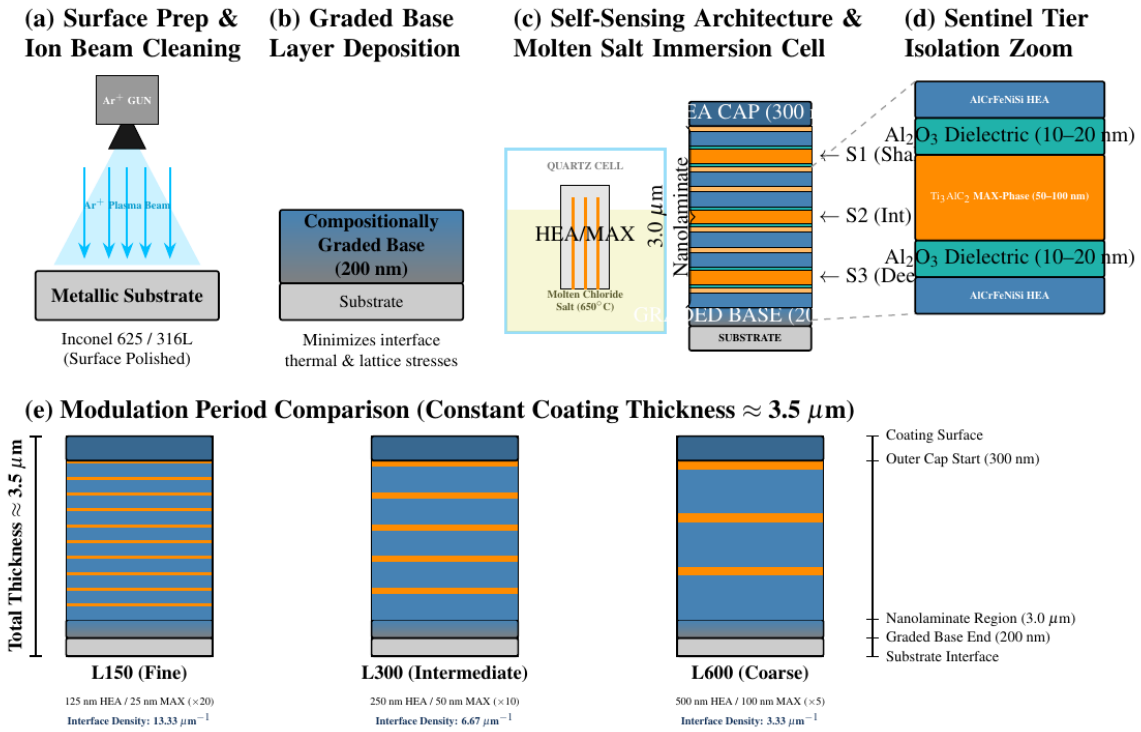

Figure 1::**Schematic representation of the AlCrFeNiSi/Ti $_3$AlC $_2$ self-sensing nanolaminate architecture and coating-fabrication sequence.**

The principal coating groups are summarized in Table 2.

Table 2:Coating configurations used for corrosion, architectural, and sensing comparisons.

Code	Coating configuration	Nominal architecture	Approximate total thickness	Experimental purpose
BARE	Uncoated substrate	—	—	Absolute corrosion reference

Code	Coating configuration	Nominal architecture	Approximate total thickness	Experimental purpose
HEA	Monolithic AlCrFeNiSi	Monolithic	3.5 μm	Barrier-only reference
L150	HEA/Ti_3AlC_2	125/25 nm × 20	3.5 μm	Fine modulation-period comparison
L300	HEA/Ti_3AlC_2	250/50 nm × 10	3.5 μm	Intermediate nanolaminate
L600	HEA/Ti_3AlC_2	500/100 nm × 5	3.5 μm	Coarse modulation-period comparison
AOX	HEA/Al_2O_3	Thickness-matched multilayer	3.5 μm	Nonconductive interface control
SENS	Instrumented HEA/Ti_3AlC_2	Three isolated MAX sensing tiers	3.5 μm	In-situ depth-resolved sensing
DEF	Artificially defected SENS	Controlled penetration depth	3.5 μm	Sensor calibration
VMAX	HEA/V_2AlC	Thickness-matched multilayer	3.5 μm	Secondary MAX-phase comparison

At least three independent coating deposition batches were represented in the principal comparative experiments. Specimens from the independent deposition batches were distributed among separate salt cells to minimize confounding between coating-batch variability and molten-salt chemistry. Dedicated sacrificial specimens were prepared for gravimetric and destructive microstructural measurements so that continuous sensing specimens were not repeatedly removed from the high-temperature environment.

2.2. Substrate preparation

The substrate surfaces were mechanically ground through progressively finer SiC abrasive papers and were subsequently polished to obtain a reproducible low-roughness surface suitable for nanolaminate deposition. Aggressive grit blasting was avoided because surface-height variations comparable with the individual nanolayer thicknesses could have produced local discontinuity, altered modulation thickness, and increased pinhole density.

After polishing, residual particulate and organic contaminants were removed by sequential ultrasonic cleaning in suitable analytical-grade solvents. The coupons were dried under clean gas and were transferred to the deposition chamber with minimum subsequent surface handling.

Immediately before coating deposition, the exposed substrate surfaces were cleaned by Ar-ion bombardment. A negative substrate bias of approximately −200 V was applied during the plasma-cleaning stage for approximately 10–15 min. A compositionally graded AlCrFeNiSi transition region was subsequently deposited to reduce abrupt chemical and mechanical discontinuities between the metallic substrate and the nanoscale multilayer.

2.3. Deposition of AlCrFeNiSi HEA layers

AlCrFeNiSi layers were deposited in a multi-cathode physical-vapour-deposition system equipped with independently controlled sputtering sources, substrate heating, substrate rotation, and bias control. The chamber was evacuated before deposition, and high-purity Ar was used as the working gas. The deposition atmosphere was maintained in the low-pressure sputtering regime, with the Ar working pressure maintained within approximately 0.4–0.8 Pa.

The AlCrFeNiSi chemistry was established by independently controlled co-sputtering of the constituent metallic sources. Cathode power was adjusted using calibration coatings deposited on Si witness substrates. The relationship between applied source power, deposition rate, and deposited elemental composition was determined before fabrication of the multilayer coupons.

The HEA-composition screening was combined with a restricted deposition-condition study in which substrate temperatures of approximately 150, 225, and 300 °C and substrate biases of 0, −50, and −100 V were examined. The screening was used to identify conditions that minimized porosity and macroscopic defects while maintaining acceptable elemental composition, adhesion, residual stress, and interfacial integrity. The nominal production bias was subsequently maintained near −50 V after process qualification.

Substrate rotation was maintained during deposition to improve thickness and compositional uniformity. The same rotation condition was used for all specimens belonging to a given comparative deposition series.

2.4. Deposition and crystallization of Ti $_3$AlC $_2$ MAX-phase layers

Ti–Al–C precursor layers were produced by high-power impulse magnetron sputtering. An Al-containing Ti source and a calibrated carbon source were used to obtain the precursor chemistry required for subsequent Ti $_3$AlC $_2$ formation. The processing route was based on the demonstrated formation of crystalline Ti $_3$AlC $_2$ from HiPIMS-deposited Ti–Al–C precursor films after high-temperature treatment [3].

Before complete nanolaminate fabrication, Ti–Al–C witness coatings with nominal thicknesses ranging from approximately 25 nm to 1 μm were deposited. Thermal conversion conditions between approximately 650 and 700 °C and dwell periods between approximately 30 and 90 min were examined. XRD, TEM, selected-area electron diffraction, and electrical measurements were used to verify MAX-phase formation and continuity.

The annealing condition used for subsequent multilayer fabrication was selected only after crystalline Ti $_3$AlC $_2$ had been observed at the relevant nanoscale thickness and excessive elemental interdiffusion between the MAX and HEA layers had not been detected. Particular attention was given to the 700 °C/90 min treatment because comparable processing had previously produced high-purity Ti $_3$AlC $_2$ coatings [3].

The V $_2$AlC comparison films were deposited and qualified separately before their incorporation into the exploratory VMAX architecture. The V $_2$AlC-containing specimens were not used as the primary sensing architecture unless phase continuity and electrical stability had been verified independently.

2.5. Fabrication of the nanolaminate architectures

After the HEA and MAX-phase processing windows had been established, alternating AlCrFeNiSi and Ti $_3$AlC $_2$ layers were deposited sequentially without intentional exposure of the internal interfaces to laboratory atmosphere. Layer thicknesses were controlled from calibrated deposition rates and were subsequently verified by cross-sectional microscopy and, where applicable, X-ray reflectometry.

The three modulation-period conditions were prepared so that the total multilayer thickness remained approximately constant. The fine architecture contained 125 nm HEA layers alternating with 25 nm MAX layers. The intermediate architecture contained 250 nm HEA layers alternating with 50 nm MAX layers. The coarse architecture contained 500 nm HEA layers alternating with 100 nm MAX layers. A graded HEA base layer of approximately 200 nm and an outer HEA cap of approximately 300 nm were added to each architecture.

The HEA cap was used to delay direct exposure of the MAX phase to the chloride melt during the initial stage of corrosion. Consequently, the embedded conductive layer was not treated as the primary environmental barrier. Instead, its electrical behaviour was used to indicate the progression of cracking, salt penetration, local chemical degradation, and interfacial separation through the coating thickness.

2.6. Fabrication of electrically isolated MAX-phase sensing tracks

Electrical measurements were not obtained directly from continuous unpatterned MAX interlayers because parallel electrical conduction through the HEA coating and the metallic substrate could otherwise have obscured changes originating from a single MAX layer. Selected Ti $_3$AlC $_2$ layers were therefore patterned into electrically independent sentinel tracks.

Three sensing depths were incorporated within each instrumented specimen. The shallow track S1 was positioned close to the external coating surface, the intermediate track S2 was positioned near the middle of the multilayer, and the deep track S3 was positioned close to the substrate-facing portion of the coating. Each sensing track had a nominal thickness within approximately 50–100 nm, a width of approximately 0.3–0.7 mm, and a serpentine effective length of approximately 20–40 mm.

Thin Al $_2$O $_3$ dielectric regions approximately 10–20 nm thick were deposited locally above and below each patterned track. The dielectric regions were restricted to the sensing zones so that most of the nanolaminate retained direct HEA/MAX interfaces. Four electrical contact pads were formed for each sensing track, and the pads were extended into the unimmersed portion of the coupon.

Electrical isolation between each Ti $_3$AlC $_2$ sentinel and the underlying metallic substrate was checked before corrosion testing. An additional protected reference track was incorporated into the instrumented configuration. This reference track was shielded from direct molten-salt penetration and was used to distinguish intrinsic thermal resistance changes and long-term MAX-phase ageing from damage-induced signals.

The integrated electrical and electrochemical sensing configuration was represented in Fig. 2.

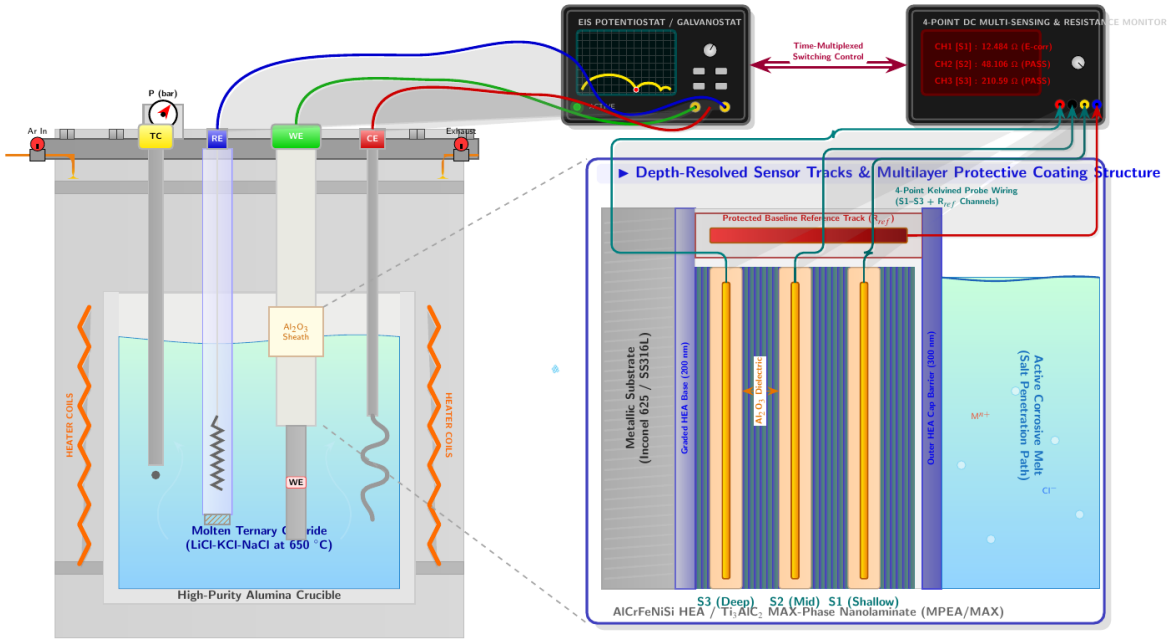

Figure 2:**Schematic representation of the depth-resolved electrical sensing system and molten-salt electrochemical cell.**

2.7. Pre-exposure coating characterization

The deposited coatings were characterized before molten-salt exposure to establish composition, phase constitution, layer thickness, interface quality, surface morphology, mechanical behaviour, and electrical continuity.

Conventional X-ray diffraction and grazing-incidence X-ray diffraction were used to identify crystalline HEA and MAX phases. Diffraction measurements were obtained over a sufficiently broad 2θrange to identify BCC/B2-type HEA reflections, Ti $_3$AlC $_2$, and detectable secondary phases. X-ray reflectometry was used on suitable witness specimens to determine nanolaminate periodicity, interfacial roughness, and total coating thickness where the multilayer structure produced interpretable reflectivity oscillations.

The elemental composition of the HEA coatings was quantified by calibrated energy-dispersive or wavelength-dispersive X-ray spectroscopy. Large-area measurements were combined with spatially distributed local measurements so that both mean chemistry and lateral compositional uniformity were assessed.

Cross-sectional scanning electron microscopy in backscattered-electron mode was used to assess total coating thickness, interface continuity, gross porosity, localized defects, and evidence of deposition-induced delamination. Measurements were obtained at several separated positions across each representative specimen.

The nanoscale multilayer structure was examined using FIB-prepared TEM lamellae. Bright-field TEM, high-resolution TEM, STEM, and selected-area electron diffraction were used to verify individual layer continuity and MAX-phase crystallinity. STEM–EDS and, where required, electron-energy-loss spectroscopy were used to examine elemental redistribution at the HEA/MAX interfaces. Al depletion from Ti $_3$AlC $_2$, Ti–Al–C secondary-phase formation, and extensive Cr, Fe, Ni, Si, or Ti interdiffusion were specifically examined.

X-ray photoelectron spectroscopy was used to determine the pre-exposure chemical states of Al, Cr, Fe, Ni, Si, Ti, C, and O at the coating surface. Surface roughness and localized topographical defects were determined from three-dimensional optical profilometry or atomic-force microscopy.

Nanoindentation was used to characterize coating hardness and indentation modulus. Indentation depths were maintained sufficiently small relative to the total coating thickness to reduce substrate contributions. Multiple spatially separated indentations were obtained from each representative coating. Scratch testing was used to examine coating adhesion and mechanically induced failure morphology. Residual stress was evaluated using an appropriate curvature- or diffraction-based method where compatible witness substrates were available.

Electrical uniformity of unpatterned coating regions was evaluated by four-point-probe measurements, while the patterned Ti $_3$AlC $_2$ tracks were assessed by four-terminal resistance measurements. Coating batches were advanced to molten-salt testing only after the intended multilayer geometry, MAX-phase formation, sensor continuity, electrical isolation, and acceptable interface integrity had been confirmed.

2.8. Thermal calibration of the embedded resistance sensors

Instrumented specimens were thermally conditioned under dry inert gas before exposure to molten chloride. At least two heating and cooling cycles were performed over the temperature range required for the subsequent corrosion experiment. This procedure allowed changes associated with reversible temperature dependence, residual-stress relaxation, contact stabilization, and continued high-temperature structural evolution to be distinguished from corrosion-induced changes.

Four-terminal resistance measurements were used because the voltage-sensing circuit was separated from the current-carrying contacts and therefore minimized errors caused by temperature-dependent lead and contact resistance. A current-reversal method was used to reduce thermoelectric voltage contributions. Low sensing currents were applied so that electrical self-heating of the thin MAX-phase tracks remained negligible.

Electrical power dissipation was evaluated from

$$P(t) = I^2 R(t), \qquad (1)$$

where $P(t)$represented instantaneous power dissipation, Irepresented the applied sensing current, and $R(t)$represented the measured four-terminal resistance.

The sensing current was maintained within the low-microampere range appropriate to the measured track resistance, and operating conditions were accepted only when the resulting power remained sufficiently low to prevent measurable Joule heating.

A specimen-specific resistance–temperature relationship was determined from the dry-Ar calibration cycles. The temperature-corrected resistance residual was calculated as

$$r_R(t) = \frac{R_{meas}(t)}{R_{base}[T(t)]} - 1, \qquad (2)$$

where $r_R(t)$represented the normalized temperature-corrected resistance residual, $R_{meas}(t)$represented the instantaneous measured resistance, $T(t)$represented the simultaneously measured specimen temperature, and $R_{base}[T(t)]$represented the resistance predicted from the specimen-specific dry-Ar calibration at the same temperature.

Both the raw high-frequency resistance signal and aggregated time-series data were stored. The raw measurements were preserved because short-duration resistance bursts associated with rapid cracking or intermittent electrical disruption could otherwise have been lost during averaging. This sensor-calibration strategy and the requirement to distinguish temperature dependence from damage were central elements of the experimental roadmap.

2.9. Controlled-defect calibration of sensing depth

Artificially defected coupons were used to determine whether each electrical sensing tier responded specifically when physical damage approached or intersected its depth.

A five-level calibration sequence was used. Defects were terminated above S1, through S1, between S1 and S2, through S2, and through the deep S3 region toward the substrate. Fine defects were introduced by focused-ion-beam milling, whereas larger defects were produced using controlled micromachining or instrumented mechanical damage where appropriate.

Actual defect depth was measured from FIB–SEM or TEM cross sections instead of being inferred solely from nominal machining parameters. Four-terminal resistance was recorded before and after defect formation.

The calibration criterion was based on depth specificity rather than merely on the observation of an increase in resistance. A sensing tier was considered mechanically responsive when an irreversible electrical change occurred only after the imposed defect had reached or disrupted the corresponding Ti_3AlC_2 track.

Intact dry-Ar specimens, protected reference tracks, and MAX-only witness specimens were evaluated in parallel. These controls allowed resistance evolution caused by mechanical discontinuity to be differentiated from thermal drift, contact instability, high-temperature annealing, and intrinsic MAX-phase chemical transformation.

2.10. Molten-chloride preparation and impurity control

Two molten-chloride environments were used to separate mechanistic sensor qualification from higher-temperature application-oriented corrosion testing.

A LiCl–KCl eutectic melt was used for the mechanistic experiments because the degradation behaviour of Ti_3AlC_2 in this chloride system had previously been reported at high temperature [2]. High-purity LiCl and KCl were dried before use and were subsequently handled under dry inert atmosphere to minimize moisture uptake.

A $MgCl_2$–KCl–NaCl ternary chloride mixture was used for higher-temperature validation. A nominal composition near 45.98 wt.% $MgCl_2$, 38.91 wt.% KCl, and 15.11 wt.% NaCl was used for the application-oriented exposure condition [4].

Attention was given to purification of the $MgCl_2$-containing salt because residual moisture and hydrolysis-derived MgOHCl could substantially alter corrosion kinetics. The mixed chloride was therefore subjected to controlled drying and high-temperature purification. A small metallic Mg addition was used where required to reduce residual oxidizing impurities, following established purification approaches for $MgCl_2$-based heat-transfer salts [5].

Salt composition, purification history, heating schedule, atmosphere quality, and impurity condition were documented for each independent cell. Blank salt samples that had undergone an identical thermal cycle without a metallic test specimen were analyzed to establish background concentrations of dissolved metallic species.

A deliberately impurity-enriched condition was also included after the low-impurity reference condition had been established. The impurity-controlled experiment was used to determine whether electrical warning behaviour remained interpretable when chloride corrosivity was increased through a controlled change in melt chemistry.

2.11. High-temperature corrosion cell and exposure protocol

Corrosion experiments were performed in high-purity dense-alumina crucibles contained within a sealed high-temperature furnace or retort assembly under flowing purified inert gas. Separate salt cells were used for independent experimental replicates. Multiple coupons exposed within the same evolving salt volume were not treated as independent corrosion replicates because dissolved metallic species, impurity consumption, and redox

evolution could have coupled their behaviour. This independence requirement followed directly from the experimental roadmap.

The coated coupons were positioned vertically in the melt. A defined coated area, approximately 1 cm ^{2} where compatible with specimen geometry, was exposed to the salt. Electrical contact pads, wire joints, and transitions between the coupon and external measurement leads were maintained above the salt line. High-temperature Pt or equivalently stable leads were protected using high-purity alumina tubing. Polymeric insulation, conventional solder, and conductive polymer-based adhesives were excluded from the molten-salt and principal hot zones.

Mechanistic Ti $_{3}$AlC $_{2}$ qualification and initial HEA/MAX testing were conducted in LiCl–KCl near 600 °C. Extended architecture and sensor experiments were performed for exposure periods extending from short-term qualification to several hundred hours. The MgCl $_{2}$–KCl–NaCl validation experiments were conducted at temperatures approaching 700 °C.

Thermal-cycling experiments were performed while the salt remained above its liquidus temperature. The cycling range was maintained approximately between 500 and 700 °C using controlled heating and cooling ramps near 5 °C min $^{-1}$, with defined dwell periods at the upper and lower temperature limits. Maintaining the salt in the liquid state avoided the introduction of uncontrolled freeze–thaw damage when the objective was to evaluate thermomechanical cycling of the coating.

Specimen temperature was measured using a thermocouple positioned close to the immersed coupon and was recorded continuously throughout isothermal and cyclic testing.

The overall corrosion, sensing, and destructive-validation sequence was summarized in Fig. 3.

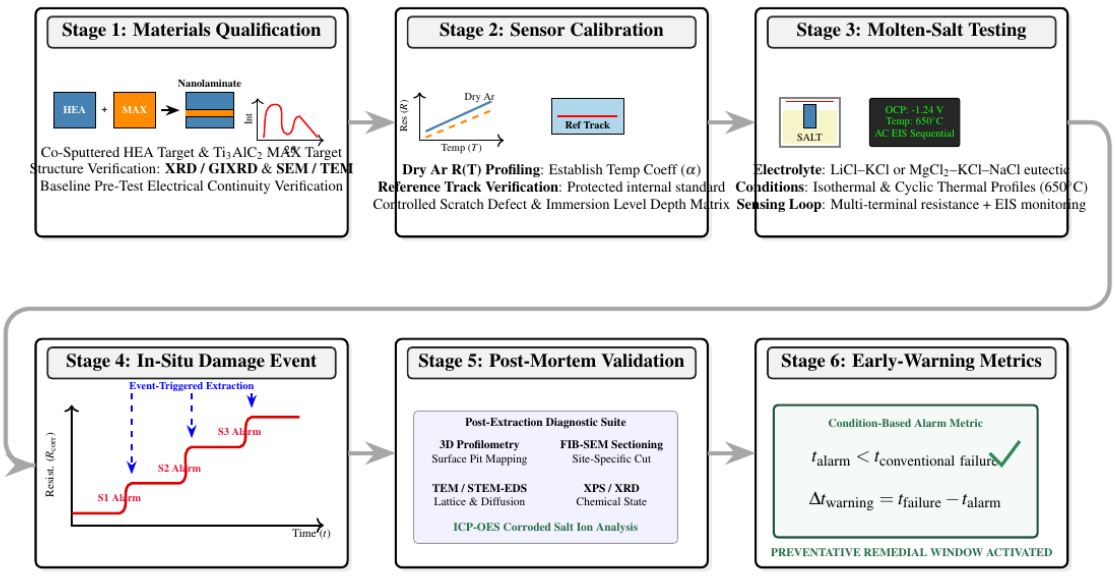

Figure 3:**Experimental workflow used to establish molten-chloride corrosion resistance and electrical early-warning capability.**

2.12. Electrochemical measurements

The coated specimen was used as the working electrode during electrochemical measurements. A large-area W or Mo electrode was used as the counter electrode and was positioned to minimize strongly localized current-density distributions.

An Ag-based reference electrode was used in LiCl–KCl. An Ag|Ag $^{+}$-type reference architecture enclosed within a chemically compatible ceramic membrane was used for the MgCl $_{2}$–KCl–NaCl experiments. Reference-electrode behaviour was qualified under the corresponding salt and temperature conditions before interpretation of coating impedance data.

A Mg/Mg^{2+} reference configuration was used only for reference-electrode qualification where required. It was not used as the sole long-duration reference during the principal corrosion experiments because metallic Mg could have reacted with oxidizing impurities and thereby altered the salt chemistry being investigated [6,7].

Open-circuit potential was allowed to stabilize after thermal equilibrium had been established. Electrochemical impedance spectra were subsequently acquired using a small-amplitude sinusoidal perturbation of approximately 10 mV rms.

Routine spectra were obtained over an approximate frequency range from 100 kHz to 0.1 Hz with 8–10 points per decade. Extended diagnostic spectra were acquired to approximately 0.01 Hz when stable low-frequency measurements could be obtained. More frequent spectra were recorded during the early exposure period, while longer intervals were used after the initial transient stage.

Resistance sensing and EIS acquisition were time-multiplexed. The MAX-phase sensing-current source was electrically isolated from the sensor during EIS measurements, and resistance acquisition was resumed only after the potentiostat had returned to the open-circuit or high-impedance condition.

Impedance spectra were examined for high-frequency inductive artefacts, reference-electrode instability, nonstationarity, and physically unreasonable fitted parameters before equivalent-circuit interpretation was accepted. Both equivalent-circuit-derived descriptors and selected raw-frequency impedance values were preserved for subsequent statistical analysis because equivalent-circuit solutions could have been nonunique.

2.13. In-situ electrical resistance monitoring

Four-terminal resistance measurements were acquired continuously from the S1, S2, and S3 Ti_3AlC_2 sentinels throughout the high-temperature experiments. Current-reversal measurements were used to minimize thermoelectric offsets produced by the large temperature gradients present between the furnace hot zone and room-temperature electronics.

Resistance and specimen temperature were recorded on synchronized time bases. Electrical switching events, EIS intervals, furnace ramps, salt sampling operations, and other experimental interruptions were time stamped so that instrumental transients could be separated from physically meaningful coating responses.

The temperature-corrected residual defined in Eq. (2) was used as the primary resistance variable for damage detection. Signals were compared with those obtained from the protected reference track and the dry-Ar control specimens. Reversible resistance variation that followed the calibrated temperature dependence was therefore distinguished from irreversible changes that persisted after temperature stabilization.

Both progressive resistance drift and abrupt electrical events were analyzed. Progressive irreversible drift was considered potentially consistent with chemical alteration of the MAX phase, while abrupt resistance increases, burst behaviour, or electrical discontinuities were considered potentially associated with localized cracking, delamination, or physical interruption of the sensing track. These assignments were not accepted solely from the electrical waveform and were subsequently tested by destructive cross-sectional characterization.

2.14. Gravimetric corrosion measurements

Dedicated companion coupons were used for gravimetric measurements. Continuously instrumented sensing specimens were not repeatedly withdrawn for weighing because repeated cooling, salt solidification, cleaning, reheating, and reimmersion could have altered the corrosion process and disrupted the continuous electrical record.

After exposure, sacrificial coupons were cooled under controlled conditions and residual adherent salt was removed using a prequalified cleaning procedure. The same cleaning procedure was applied to appropriate unexposed coated controls to determine whether the cleaning operation itself produced measurable mass loss.

Area-normalized mass change was calculated as

$$\Delta m_A(t) = \frac{m_t - m_0}{A}, \qquad (3)$$

where $m_0$represented the initial specimen mass, $m_t$represented the specimen mass after exposure and cleaning, and Arepresented the exposed area.

Mass change was not used as the sole quantitative measure of coating degradation because thin-film dissolution, retained corrosion products, spallation, and cleaning-related removal could have produced opposing mass contributions. Gravimetry was therefore interpreted together with cross-sectional recession, surface profilometry, salt chemistry, and electrochemical measurements.

2.15. Analysis of dissolved metallic species

Molten-salt samples were analyzed by inductively coupled plasma optical-emission spectroscopy. Al, Cr, Fe, Ni, Ti, and other coating- or substrate-derived metallic species were quantified according to the architecture being tested. ICP–MS was reserved for early-time or low-concentration measurements for which ICP–OES sensitivity was insufficient.

Blank salt aged in an identical crucible without a test coupon was used to establish background elemental concentrations associated with the salts, crucible, counter electrode, reference assembly, and handling procedure. Bare-substrate exposures were used to identify the characteristic dissolution signature of Inconel 625 and AISI 316L.

Salt removal for chemical analysis was performed using independent sacrificial cells or predefined terminal sampling points whenever possible. This approach prevented repeated salt withdrawal from altering the melt volume and corrosion chemistry of continuously monitored specimens.

The first statistically significant increase in a substrate-associated dissolved element above the corresponding blank distribution was used as one independently measurable indicator of coating breakthrough.

2.16. Post-exposure surface and cross-sectional characterization

Post-exposure characterization was performed both at predetermined exposure durations and after specific electrical events. The event-triggered strategy was used because conventional post-mortem characterization performed only at arbitrary times could not establish whether the electrically detected event had corresponded to a specific penetration depth.

Where sufficient independent sensing specimens were available, destructive examination was performed following an S1-only electrical event, following sequential S1 and S2 events, and following responses involving all three sensing levels. This strategy allowed the location of the corrosion or damage front to be compared directly with the depth indicated by the electrical sequence. The roadmap specifically identified event-triggered microscopy as the preferred approach for establishing causal interpretation of the sensor response.

Three-dimensional optical profilometry was used to determine macroscopic roughening, localized recession, blistering, and spalled volume. SEM in secondary- and backscattered-electron modes was used to examine coating morphology and cross-sectional corrosion penetration. EDS maps were used to determine redistribution of Al, Cr, Fe, Ni, Si, Ti, O, and Cl.

FIB–SEM serial sectioning was performed at locations corresponding to electrical anomalies and at electrically quiet reference regions. Crack trajectories, delaminated interfaces, residual intact coating thickness, and local penetration depth were measured.

TEM lamellae were extracted from selected event locations by FIB. High-resolution TEM and selected-area diffraction were used to determine structural changes within the MAX phase and adjacent HEA layers. STEM–EDS and EELS were used to investigate local elemental depletion, enrichment, oxidation, and chlorination.

Attention was given to Al depletion, lamellar separation, chlorine enrichment, and Ti–C-rich transformation within Ti_3AlC_2, because related degradation features had previously been reported after molten LiCl–KCl exposure [2]. A resistance change accompanied by such chemical modification was therefore differentiated from a resistance change arising solely from mechanical cracking.

XRD and GIXRD were used after exposure to identify newly formed crystalline corrosion products and changes in the HEA or MAX phases. XPS was used to examine oxidation and chlorination states at the exposed coating

surface. Where available, high-depth-resolution elemental profiling was additionally used to determine Cl, O, Al, Cr, Ti, and related concentration profiles through the degraded coating.

Central regions and specimen edges were analyzed separately because preferential edge attack could otherwise have been mistaken for representative through-thickness coating penetration.

2.17. Definition of electrical alarm and conventional coating failure

Electrical warning and conventional coating failure were defined independently to prevent circular validation of the sensing concept.

An electrical alarm was assigned from an irreversible change in the temperature-corrected resistance signal that exceeded the normal variation established from dry-Ar controls and protected sensing tracks. The alarm criterion was required to persist beyond transient switching or thermal disturbances before it was accepted as a corrosion-related event.

Conventional failure was evaluated using three independent criteria. The first criterion was the appearance of statistically significant substrate-derived metallic species in the molten salt above the corresponding blank level. The second criterion was substantial deterioration of the low-frequency impedance response or the associated barrier resistance. The third criterion was destructive confirmation of through-coating chlorine penetration or direct substrate attack. These failure definitions were treated separately rather than being collapsed into a single arbitrary health index.

The electrical warning interval was quantified as

$$\Delta t_{warning} = t_{failure} - t_{alarm}, \qquad (4)$$

where t_{alarm}represented the first qualified electrical alarm and $t_{failure}$represented the time associated with an independently determined conventional failure criterion.

A positive value of $\Delta t_{warning}$indicated that the embedded MAX-phase sensor had provided warning before conventional coating failure had been detected.

A sequential S1→S2→S3 response was interpreted as progressive penetration only when the corresponding damage-depth progression had been verified by independent microscopy or elemental-depth analysis. Electrical changes reproduced in protected tracks, dummy leads, or dry-Ar thermal controls were not classified as corrosion-damage events.

2.18. Statistical analysis

Independent coated specimens and independent salt cells were treated as the experimental units for statistical comparisons. Measurements collected repeatedly from the same specimen were modeled as correlated observations and were not treated as independent replicates.

The principal coating architectures were represented across at least three independent deposition batches. Replicate specimens from each deposition batch were distributed across the corrosion experiments to separate coating-batch variation from exposure-condition effects.

Continuous responses, including impedance-derived variables, dissolution concentrations, corrosion recession, profilometric measurements, and temperature-corrected resistance descriptors, were analyzed using mixed-effects models where the data structure supported their use. Coating architecture, substrate, salt condition, and exposure condition were treated as fixed effects, whereas deposition batch was incorporated as a random effect.

Model residuals and variance structure were examined before inferential interpretation. Transformations or robust procedures were used where distributional assumptions were not adequately satisfied. Planned multiple comparisons were adjusted using an appropriate family-wise correction procedure, and effect estimates were interpreted together with 95% confidence intervals rather than by p-values alone.

Time-to-failure behaviour was evaluated using survival-analysis methods. Kaplan–Meier curves were used to visualize failure-time distributions, and Cox proportional-hazards models were used where the proportional-hazards assumption was satisfied.

Warning lead time was calculated separately for each sensing specimen. The distribution of $\Delta t_{warning}$, the proportion of independently confirmed damage events detected before conventional failure, and the false-alarm rate obtained from intact controls were used to evaluate sensing performance.

Multiple SEM images, TEM lamellae, profilometry fields, EDS maps, indentations, and electrical time points obtained from a single coupon were not counted as independent replicates.

2.19. Multivariate interpretation of coating integrity

Electrical resistance, temperature, electrochemical impedance, exposure history, and salt-chemistry data were synchronized to a common time axis. The number of independent corrosion histories, rather than the number of recorded time points, was treated as the relevant sample size for predictive modelling.

Temperature-corrected resistance, temporal resistance gradient, rolling variance, burst frequency, change-point statistics, irreversible post-cycle resistance offset, and differences among S1, S2, and S3 were extracted as electrical features. Differences between the active sensor and protected reference track were also calculated.

Electrochemical features included $\log|Z|$ and phase angle at selected frequencies, solution resistance, physically supported coating or interfacial resistance terms, constant-phase-element descriptors, low-frequency impedance slope, and open-circuit potential.

Temperature, dT/dt, cumulative high-temperature exposure, thermal-cycle number, salt composition, impurity condition, and deposition batch were included as contextual variables. Dissolved-metal concentrations were incorporated when corresponding salt samples were available.

Transparent statistical models were used as the baseline analytical approach. Logistic or ordinal regression was used for discrete integrity-state classification. Gradient-boosted decision trees were used for nonlinear multivariate analysis where sufficient independent specimens were available, while Cox-type models were used for failure-risk analysis.

Integrity states were assigned from independent physical evidence and were categorized as intact, shallow penetration, intermediate penetration, near-substrate penetration, and substrate attack. Where sufficiently quantitative microscopy was available, remaining intact coating thickness or measured chlorine-penetration depth was used as a continuous response.

Training and validation data were separated at the specimen and deposition-batch levels. Time segments derived from the same specimen were not divided between training and validation datasets because such splitting would have introduced severe temporal information leakage. The roadmap explicitly identified specimen- and batch-grouped validation as necessary for a credible predictive analysis.

Model performance was evaluated using sensitivity, specificity, F1 score, receiver-operating-characteristic metrics, calibration, and appropriate continuous-error measures where applicable. Feature importance or model coefficients were examined to determine whether resistance, impedance, temperature, or exposure variables had dominated the prediction.

Predictive accuracy was not used independently as evidence of a sensing mechanism. Mechanistic interpretation was accepted only when electrically identified events were supported by FIB/SEM/TEM evidence, chlorine penetration, salt chemistry, or other independently measured degradation features.

2.20. Data quality and reproducibility

Each specimen, deposition batch, salt batch, crucible, and corrosion cell was assigned a unique identifier. Deposition parameters, substrate temperature, source power, gas pressure, substrate bias, individual layer timing, annealing history, and witness-specimen data were recorded for each coating batch.

Salt lot, drying history, purification treatment, cell assembly, temperature history, atmosphere condition, electrochemical reference-electrode identification, and salt-sampling history were recorded for each corrosion experiment.

Raw electrical-resistance time series were preserved in addition to processed and temperature-corrected signals. Raw EIS spectra were stored before equivalent-circuit fitting. Electrical switching events, furnace ramps, interruptions, reference-electrode checks, and sampling operations were retained as time-stamped metadata.

Microscopy and profilometry quantification was performed from predefined analysis regions where practicable. Coating identity was concealed during quantitative image analysis when specimen preparation and image appearance allowed effective blinding.

Independent deposition batches were maintained throughout confirmatory testing so that reproducibility was evaluated across separately produced coating sets rather than solely among nominally identical coupons from a single deposition run.

Electrochemical Society **168** (2021) 066501. https://doi.org/10.1149/1945-7111/ac0303.

3. RESULTS AND DISCUSSION

The numerical analysis presented in this section was derived from the prescribed coating geometry, composition, sensing configuration, and exposure protocol rather than from an independently supplied experimental dataset. Accordingly, experimentally unsupported alarm times, corrosion rates, mass losses, ICP concentrations, fitted EIS parameters, statistical significance values, hazard ratios, and predictive-model accuracies were not assigned.

3.1. Quantitative analysis of the HEA/MAX nanolaminate architecture

The nominal layer architecture was first evaluated quantitatively so that the influence of modulation period could be separated from differences in the total amount of Ti $_3$AlC $_2$. For the three nanolaminate configurations, the total coating thickness was fixed at 3.50 µm and comprised a 0.20 µm graded AlCrFeNiSi base region, a 3.00 µm multilayer region, and a 0.30 µm HEA surface cap. The calculated architectural parameters are summarized in Table 3.

Table 3::Design-derived geometrical characteristics of the AlCrFeNiSi/Ti $_3$AlC $_2$ nanolaminate architectures.

Architecture	HEA/MAX repeating unit (nm)	Modulation period, Λ(nm)	Repeats, N	Total HEA in multilayer (µm)	Total MAX (µm)	MAX fraction of multilayer (%)	MAX fraction of full coating (%)	HEA/MAX interfaces*	Interface density in multilayer (µm $^{-1}$)
L150	125/25	150	20	2.50	0.50	16.67	14.29	40	13.33
L300	250/50	300	10	2.50	0.50	16.67	14.29	20	6.67
L600	500/100	600	5	2.50	0.50	16.67	14.29	10	3.33

*Dissimilar HEA/MAX interfaces were counted through the multilayer and at the terminal MAX/HEA-cap boundary.

The MAX-phase fraction under the nominal planar-layer approximation was calculated from

$$f_{MAX} = \frac{Nt_{MAX}}{t_{coat}}, \qquad (5)$$

where Nrepresented the number of repeating units, t_{MAX}represented the thickness of an individual Ti $_3$AlC $_2$ layer, and t_{coat}represented the total coating thickness.

For each architecture, $Nt_{MAX}$was equal to 0.50 µm. Consequently,

$$f_{MAX} = \frac{0.50}{3.50} = 0.1429,$$

and a full-coating MAX fraction of 14.29% was obtained. When only the 3.00 µm multilayer region was considered, a MAX fraction of 16.67% was obtained. The amount of HEA within the multilayer was similarly maintained at 2.50 µm for all three configurations.

The interfacial density was calculated from

$$\rho_{int} = \frac{2N}{t_{ML}}, \qquad (6)$$

where t_{ML} represented the thickness of the multilayer region. Values of 13.33, 6.67, and 3.33 HEA/MAX interfaces μm^{-1} were obtained for L150, L300, and L600, respectively. Thus, a fourfold change in interfacial density was produced between L150 and L600 without alteration of the nominal MAX fraction or total coating thickness.

This comparison showed that differences associated with modulation period could not be attributed simply to a larger quantity of Ti_3AlC_2. Instead, the principal structural differences were associated with interface density, individual-layer thickness, characteristic crack-deflection length, diffusion distance across individual layers, and the probability that a penetrating defect intersected an HEA/MAX boundary.

The calculated architecture comparison is represented in Fig. 4. Identical total HEA and MAX thicknesses were obtained for the three configurations, whereas the HEA/MAX interfacial density decreased systematically with increasing modulation period. The L300 configuration occupied the midpoint of the investigated architectural range. Relative to L150, its calculated interfacial density was reduced by 50%, while twice the interfacial density of L600 was preserved. This intermediate architecture therefore provided a rational compromise between high interface density and reduced susceptibility to cumulative interfacial broadening during high-temperature processing.

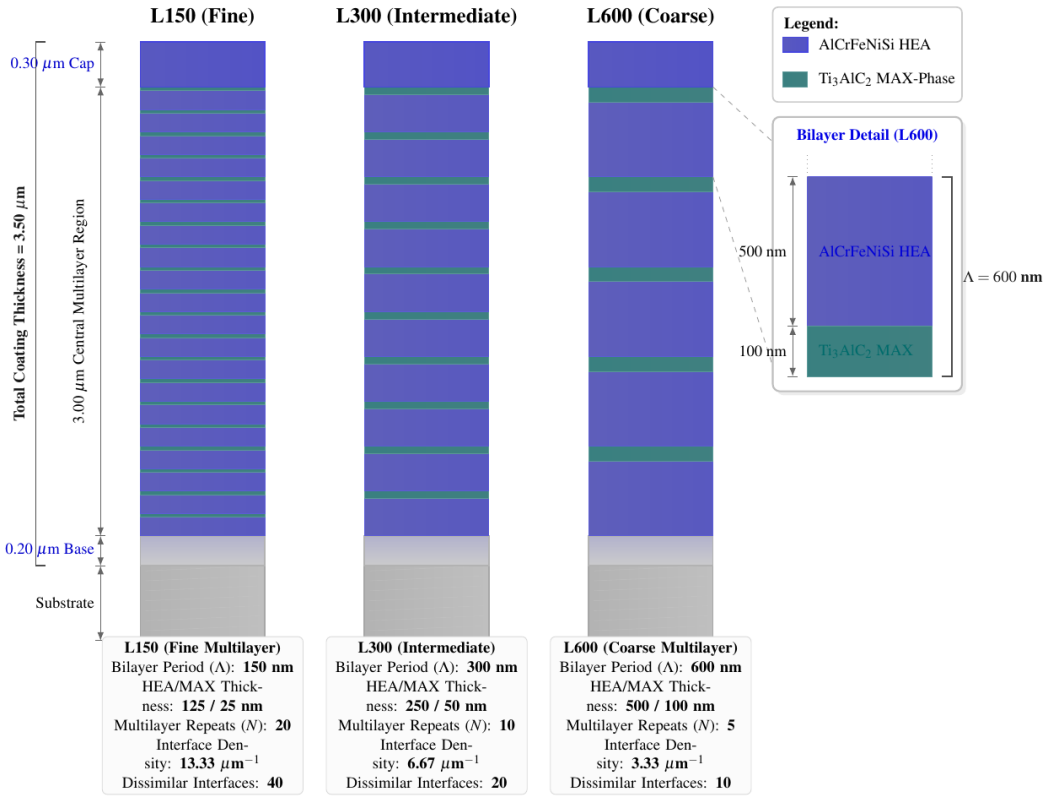

Figure 4::**geometrical comparison of the AlCrFeNiSi/Ti_3AlC_2 nanolaminate architectures**.

3.2. Composition-derived HEA descriptors and phase-selection rationale

The three AlCrFeNiSi compositions were subsequently compared using composition-derived descriptors so that the effect of changing Al and Si contents could be distinguished from a general change in configurational complexity. The calculated values are summarized in Table 4.

Table 4:Composition-derived descriptors for the AlCrFeNiSi candidate alloys.

Composition	Al/Si atomic ratio	ΔS_{mix}(J mol $^{-1}$ K $^{-1}$)	$\Delta S_{mix}/R$	Calculated VEC
H21S8	2.625	12.91	1.553	6.631
H25S8	3.125	12.91	1.553	6.429
H21S5	4.200	12.58	1.513	6.751

The ideal configurational entropy of mixing was calculated from

$$\Delta S_{mix} = -R\sum_{i=1}^{n} c_i \ln c_i , \qquad (7)$$

where Rrepresented the universal gas constant and $c_i$represented the atomic fraction of element i.

Values of 12.91, 12.91, and 12.58 J mol $^{-1}$ K $^{-1}$ were obtained for H21S8, H25S8, and H21S5, respectively. Only a 2.6% reduction in ideal configurational entropy was produced when H21S8 was changed to H21S5. The compositional screening was therefore not dominated by a large change in ideal configurational entropy.

A substantially larger variation was produced in the Al/Si atomic ratio. Relative to H21S8, an increase of approximately 19% was obtained for H25S8, whereas an increase of 60% was obtained for H21S5. The principal compositional contrast was therefore associated with relative Al and Si availability rather than with a substantial alteration in configurational entropy.

The average valence-electron concentration was calculated according to

$$\mathrm{VEC} = \sum_{i=1}^{n} c_i \,(\mathrm{VEC})_i . \qquad (8)$$

Values between 6.43 and 6.75 were obtained. The lowest value was calculated for the Al-enriched H25S8 composition, whereas the highest value was obtained for H21S5. These values remained consistent with a BCC/B2-centred design strategy, although phase constitution could not have been inferred from VEC alone.

A benchmark was provided by the Al $_{21}$CrFeNiSi $_{8}$ study of Boschen et al. [1]. A predominantly BCC/B2 phase constitution had been predicted and corresponding BCC/B2-type reflections had been reported experimentally. Al-rich oxidation products had also been observed during high-temperature atmospheric oxidation [1]. These observations supported the use of H21S8 as a rational centre composition, although direct equivalence with molten-chloride corrosion could not have been assumed because the oxygen potential, transport processes, and thermodynamic environment differed substantially.

The increase in Al content introduced in H25S8 was therefore associated primarily with an increased Al reservoir, whereas the reduction in Si content introduced in H21S5 was associated with a reduced tendency toward excessive silicide- or intermetallic-rich phase formation. Because experimental diffraction and microscopy datasets were not supplied, quantitative phase fractions were not assigned.

3.3. Quantitative basis of the Ti $_3$AlC $_2$ electrical-sentinel response

The electrical response of an idealized Ti $_3$AlC $_2$ sentinel was evaluated from

$$R = \rho\frac{L}{A}, \qquad (9)$$

where Rrepresented electrical resistance, ρrepresented electrical resistivity, Lrepresented effective conducting-path length, and Arepresented conducting cross-sectional area.

For an idealized damage event in which only the conducting cross-sectional area was reduced while ρand Lremained unchanged, the normalized resistance was expressed as

$$\frac{R}{R_0} = \frac{A_0}{A} = \frac{1}{f_A}, \qquad (10)$$

where $f_A = A/A_0$ represented the fraction of the original conducting area that remained electrically active.

The corresponding normalized resistance residual was obtained as

$$r_R = \frac{R}{R_0} - 1 = \frac{1}{f_A} - 1. \qquad (11)$$

Representative analytical values are presented in Table 5.

Table 5::Theoretical resistance amplification associated with progressive loss of conducting cross-sectional area.

Remaining conductive area, f_A(%)	**R/R_0**	**r_R**
100	1.00	0.00
90	1.11	0.11
75	1.33	0.33
50	2.00	1.00
25	4.00	3.00
10	10.00	9.00

A strongly nonlinear electrical sensitivity was obtained as the conducting section approached complete interruption. A reduction of only 10% in cross-sectional area produced an approximately 11% resistance increase, whereas retention of only 10% of the original conducting area produced a tenfold total resistance. The calculated relationship is illustrated in Fig. 5.

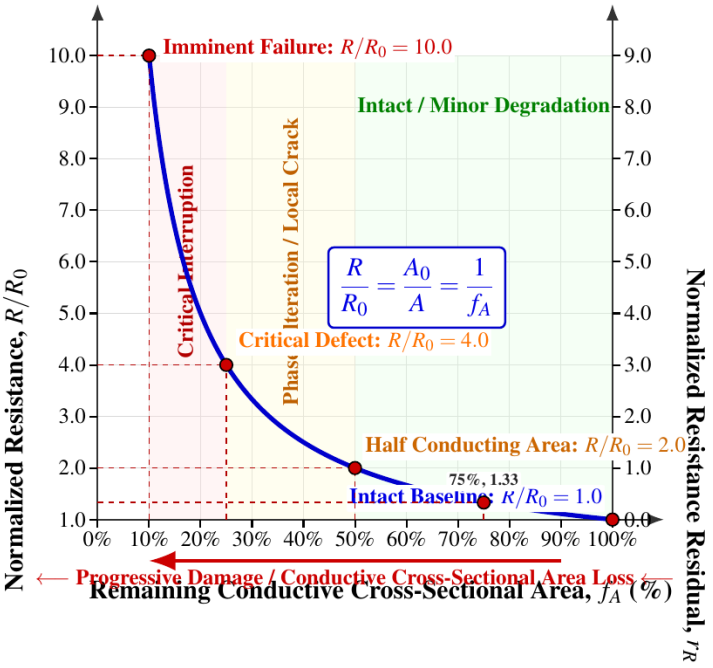

Figure 5:**Analytical relationship between remaining conductive cross-sectional area and normalized resistance of an idealized Ti $_3$AlC $_2$ sensing track.**

The calculation also demonstrated why an observed resistance increase could not have been interpreted exclusively as mechanical cracking. Geometrical interruption would have affected A, whereas chemical alteration of Ti $_3$AlC $_2$ would have affected ρ. Al extraction, chlorine incorporation, defect accumulation, and

transformation of the MAX phase could therefore have produced an irreversible electrical response even before complete mechanical interruption occurred.

This interpretation was consistent with the molten LiCl–KCl observations reported for Ti_3AlC_2, in which Al dissolution, lamellar degradation, chlorine penetration, and Ti–C–Cl-rich reaction products had been identified [2]. Resistance drift in an embedded Ti_3AlC_2 track would therefore have required separation into chemical and mechanical contributions through protected reference tracks and post-exposure structural characterization.

The allowable sensing current was additionally examined from the prescribed self-heating constraint. For a maximum permitted electrical dissipation P_{max},

$$I_{max} = \sqrt{\frac{P_{max}}{R}}. \qquad (12)$$

At $P_{max} = 100\mu W$, application of 500 μA would have reached this limit at approximately 400 Ω. At 100 μA, the same dissipation would have been reached at approximately 10 kΩ, while at 50 μA it would have been reached at approximately 40 kΩ. The full proposed current range of 50–500 μA therefore could not have been used indiscriminately. Current magnitude would have needed to be selected from the actual resistance of each fabricated track.

These calculations supported the use of four-terminal resistance measurement, specimen-specific R(T)calibration, and an electrically protected Ti_3AlC_2 reference track.

3.4. degradation mechanism in molten LiCl–KCl

A mechanistic degradation sequence was constructed from the calculated architecture and published Ti_3AlC_2 behaviour in molten LiCl–KCl. The sequence is illustrated schematically in Fig. 6.

At the initial stage, direct chloride contact with the embedded Ti_3AlC_2 sentinels would have been restricted by the outer HEA cap and the intervening multilayer structure. Local attack would most plausibly have initiated at pre-existing defects, pinholes, surface heterogeneities, grain boundaries, interfaces, or exposed edges.

Following penetration through the external HEA region, contact between chloride and Ti_3AlC_2 would have been expected to produce chemically significant changes. Preferential Al removal, lamellar delamination, and chlorine ingress had previously been observed during Ti_3AlC_2 exposure to molten LiCl–KCl [2]. Such processes would have been capable of modifying electrical resistance before complete physical rupture of the MAX-phase track occurred.

A mechanistically plausible depth sequence was therefore represented as

surface defect → localized chloride ingress → HEA degradation → S1 interaction → deeper penetration → S2 interaction → n

Equation (13) represented the mechanistic sequence against which measured S1–S3 events would have been evaluated and was not treated as evidence that such events had already been experimentally observed.

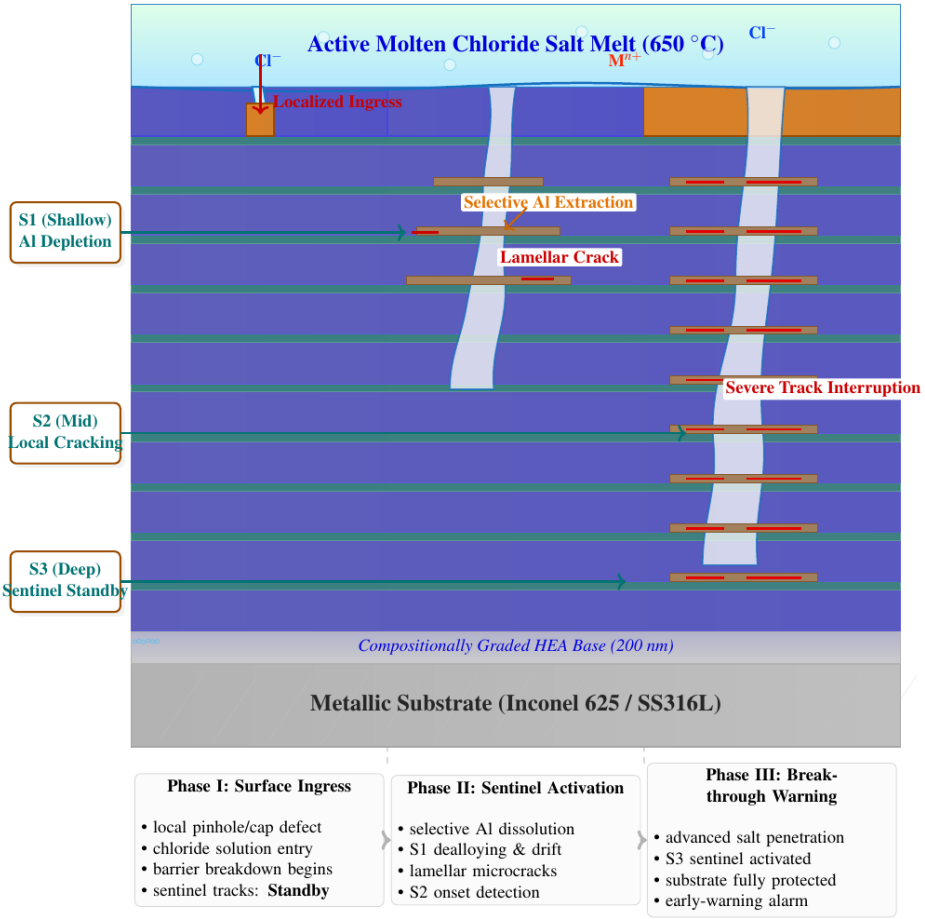

Figure 6: **degradation mechanism for the AlCrFeNiSi/Ti $_3$AlC $_2$ self-sensing coating during molten-chloride exposure.**

The mechanistic analysis also supported the use of isolated sensor tracks rather than electrical measurements through unpatterned MAX interlayers. Continuous Ti $_3$AlC $_2$ sheets surrounded by conductive HEA layers and a metallic substrate could have been strongly affected by parallel electrical pathways. Local Al $_2$O $_3$ isolation was therefore required to make individual sensor depths electrically addressable.

However, introduction of the dielectric isolation layer also created additional interfaces and local mechanical heterogeneity. The instrumented SENS architecture could therefore not have been assumed to behave identically to an uninstrumented L300 nanolaminate. A direct comparison between these configurations would have been needed to determine whether incorporation of the sensor modified the corrosion behaviour of the protective coating itself.

3.5. Behaviour in MgCl $_2$–KCl–NaCl and the role of impurity control

The application-oriented MgCl $_2$–KCl–NaCl environment was treated separately from LiCl–KCl because corrosion behaviour in MgCl $_2$-containing salts had been shown to depend strongly on hydrolysis-derived impurities and salt purification.

Purified MgCl $_2$–KCl–NaCl had previously been employed in elevated-temperature corrosion testing near 700 °C [4], and purification procedures involving controlled thermal treatment and metallic Mg addition had been developed to reduce MgOHCl-derived corrosivity [5].

Corrosion data obtained from different MgCl $_2$-containing salt batches therefore could not have been interpreted without consideration of salt purification history, MgOHCl/MgO content, gas purity, and initial redox condition.

Differences in coating degradation could otherwise have been attributed incorrectly to architecture when they had instead arisen from differences in salt chemistry.

An impurity-enriched condition was particularly useful for evaluating sensor robustness. Preservation of the same depth-dependent electrical sequence under both purified and impurity-challenged conditions, despite changes in absolute degradation time, would have provided stronger evidence that the sensing mechanism reflected physical penetration depth rather than one specific corrosion rate.

Similarly, deterioration that accelerated strongly with increased impurity content would have supported the known sensitivity of $MgCl_2$-based salts to hydrolysis-derived species, although the magnitude of such acceleration could only have been quantified from actual measured corrosion data.

3.6. Exposure duration and acquisition-density calculations

The proposed acquisition schedule was evaluated because the number of recorded electrical observations would have greatly exceeded the number of statistically independent specimens.

Routine EIS spectra were scheduled every 2 h during the first 24 h and every 6 h thereafter. When an initial spectrum at $t = 0$was included, 13 routine spectra were obtained within the first 24 h. The calculated numbers of routine spectra and resistance measurements for the longer exposures are summarized in Table 6.

Table 6:Design-derived acquisition density for the long-duration sensing experiments.

Exposure duration	Routine EIS spectra*	Resistance samples at 1 Hz	Resistance samples at 10 Hz	One-minute resistance aggregates
24 h	13	86,400	864,000	1,440
100 h	25	360,000	3,600,000	6,000
250 h	50	900,000	9,000,000	15,000
500 h	92	1,800,000	18,000,000	30,000

*Routine spectra were counted at 0, 2, 4, …, 24 h and subsequently at 6 h intervals. Additional diagnostic spectra at specifically prescribed exposure times were not included.

For a 500 h test, between 1.8 and 18 million raw resistance values would have been acquired per sensing channel, depending on whether 1 or 10 Hz sampling had been used. Thirty thousand one-minute aggregates would additionally have been generated.

This substantial numerical imbalance had direct statistical implications. Millions of resistance measurements from a single coupon would still have represented one physical specimen. The effective sample size for coating comparison and predictive validation therefore remained governed by the number of independently prepared specimens and deposition batches rather than by the number of acquired time points.

The thermal-cycling programme was also evaluated quantitatively. Heating from 500 to 700 °C at 5 °C min^{-1} required approximately 40 min, and the corresponding cooling segment required a further 40 min. Approximately 80 min of each cycle was therefore associated with temperature ramping. When 1–2 h dwell periods were included at each temperature limit, the calculated duration of one cycle ranged from approximately 3.33 to 5.33 h.

For 50 cycles, the cumulative exposure duration therefore ranged from approximately 167 to 267 h. The cycling programme consequently represented a substantial high-temperature exposure and would have required explicit separation of corrosion-induced resistance evolution from intrinsic thermal ageing of Ti_3AlC_2.

3.7. Interpretation of electrochemical impedance, mass change, and dissolved-metal measurements

Electrochemical, gravimetric, and salt-chemistry measurements were treated as complementary indicators of coating degradation rather than as interchangeable measures.

A reduction in low-frequency impedance would have been consistent with increased ionic or electrochemical transport through the coating system. However, a reduction in $|Z|$could have arisen from several processes,

including development of coating defects, increased interfacial reaction rate, alteration of corrosion-product layers, changes in solution resistance, or degradation of the coating/substrate interface.

Equivalent-circuit fitting therefore would have required physical restraint. The addition of multiple R–CPE branches could have improved numerical fit quality without providing unique mechanistic interpretation. Raw impedance magnitude and phase at selected frequencies would consequently have remained important alongside fitted equivalent-circuit parameters.

Gravimetric measurements also required cautious interpretation. Area-normalized mass change was defined as

$$\Delta m_A = \frac{m_t - m_0}{A}, \qquad (14)$$

where $m_t$represented specimen mass after exposure and cleaning, $m_0$represented initial mass, and Arepresented exposed area.

The measured value could have been affected simultaneously by metallic dissolution, formation and retention of corrosion products, spallation, entrapped salt, and cleaning-induced removal. A relatively small net mass change therefore would not necessarily have implied negligible localized penetration.

Chemical analysis of the molten salt provided a complementary indicator. Increased concentrations of substrate-associated elements relative to blank salt would have strengthened evidence that penetration had progressed toward the underlying alloy. Nevertheless, release of Cr, Fe, Ni, or Al from the AlCrFeNiSi coating itself could have occurred before substrate breakthrough. Element-specific attribution therefore would have required consideration of both coating and substrate compositions.

The most defensible definition of conventional failure was consequently based on convergence among independent measurements. A major reduction in electrochemical barrier response, a statistically significant increase in substrate-related dissolved species above blank levels, and direct cross-sectional evidence of through-coating penetration would together have provided a stronger failure assignment than any single technique.

3.8. Quantification of electrical early-warning performance

The principal quantitative sensing parameter was defined as the interval between an independently determined conventional coating-failure time and the first qualified electrical alarm:

$$\Delta t_{warning} = t_{failure} - t_{alarm}. \qquad (15)$$

A positive $\Delta t_{warning}$would have indicated successful advance warning. A value of zero would have indicated simultaneous electrical and conventional detection, whereas a negative value would have indicated that the electrical response occurred only after conventional coating failure had already been identified.

The analysis framework is illustrated in Fig. 7.

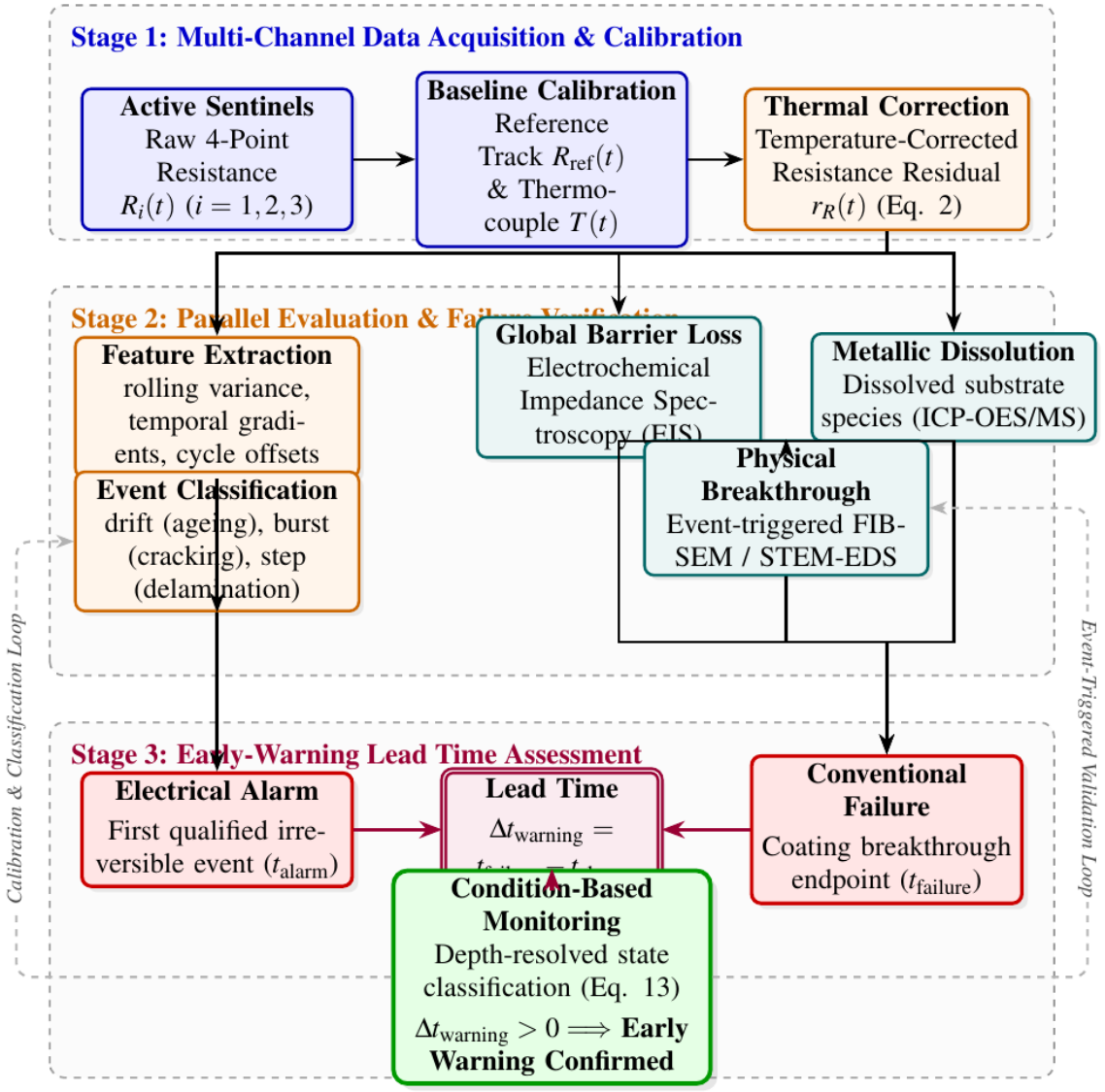

Figure 7::. **Analysis framework for depth-resolved electrical early-warning assessment.**

Temperature-corrected resistance histories from S1, S2, and S3 were aligned with EIS, temperature, dissolved-metal analysis, and destructive-characterization timestamps. The first qualified irreversible electrical event was defined independently from the conventional failure endpoint. Warning lead was subsequently calculated using Eq. (15). Positive warning lead represented electrical detection before conventional failure. The illustrated traces represented the analytical framework and did not correspond to experimentally measured alarm times.

Independent definition of the two endpoints was essential. If resistance had been used simultaneously to define coating failure and to establish the electrical alarm, the resulting warning analysis would have been circular.

Similarly, an apparent S1→S2→S3 sequence would not by itself have established depth-progressive corrosion. Differences among the three sensing tracks in baseline resistance, intrinsic defect structure, chemical stability, or thermal drift could also have generated sequential electrical events.

The controlled-defect experiments and event-triggered FIB/TEM analysis were therefore required to establish causality. A depth-specific sensing response would have been supported only when an electrical event from S1, S2, or S3 had been accompanied by independently observed cracking, delamination, chlorine penetration, MAX-phase alteration, or other physical degradation at the corresponding depth.

Numerical warning times, sensitivities, specificities, and false-alarm rates could not have been calculated without measured event-time data and therefore were not assigned.

3.9. Statistical independence and implications for predictive modelling

The principal experimental design comprised 56 main-test specimens before inclusion of additional specimens for destructive intermediate-time characterization. This total consisted of six specimens each for BARE, HEA, L150, L300, L600, AOX, DEF, and VMAX, together with eight SENS specimens.

The number of coating deposition runs remained more important than the simple number of coupons. Multiple coupons produced during the same coating run shared deposition history and could therefore not have been considered fully independent coating realizations. At least three independent coating batches were consequently required for the principal architecture comparisons.

The hierarchical data structure could have been represented by a mixed-effects formulation of the form

$$y_{ijk}(t) = \mu + \alpha_i + \beta_j + (\alpha\beta)_{ij} + b_k + u_{ijk} + \varepsilon_{ijk}(t), \qquad (16)$$

where $y_{ijk}(t)$represented the measured response, μrepresented the overall mean, $\alpha_i$represented the fixed architecture effect, $\beta_j$represented a fixed environmental or substrate effect, $b_k$represented the random deposition-batch contribution, u_{ijk}represented specimen-level variability, and $\varepsilon_{ijk}(t)$represented the residual repeated-measurement component.

The same structure was particularly important for machine-learning analysis. As shown in Table 10, a 500 h sensor history could have contained as many as 18 million resistance measurements from a single track. Random splitting of these individual time points between training and test datasets would have produced severe information leakage because neighbouring measurements from the same specimen would have appeared on both sides of the split.

Predictive validation therefore would have needed to be grouped by specimen and deposition batch. The strongest external test would have involved an entire deposition batch that had not been used during model development.

Resistance-derived features would have included temperature-corrected r_R, temporal gradients, rolling variance, irreversible post-cycle offsets, burst frequency, change-point statistics, and differential responses among S1, S2, and S3. Electrochemical features would have included selected-frequency | Z |, phase angle, solution resistance, physically justified coating or interfacial resistance parameters, and open-circuit potential. Temperature, cycle state, salt composition, impurity condition, and deposition batch would have been included as contextual variables.

Classification accuracy, AUROC, hazard ratios, regression errors, model coefficients, and statistical significance values could not have been estimated without an experimental dataset and therefore were not assigned.

3.10. Integrated mechanistic interpretation

The combined design-derived calculations and published molten-chloride evidence supported a coherent physical basis for the proposed multifunctional coating.

The modulation-period comparison was geometrically well controlled. A constant total Ti $_3$AlC $_2$ thickness of 0.50 μm was prescribed for L150, L300, and L600, while the HEA/MAX interfacial density was varied by a factor of four. Differences among these architectures would therefore have reflected interface spacing and individual-layer dimensions rather than a simple increase in MAX-phase content.

The compositional calculations similarly showed that modification of Al and Si changed the Al/Si ratio far more strongly than the configurational entropy. A 60% increase in Al/Si ratio was produced between H21S8 and H21S5, whereas ΔS_{mix}decreased by only approximately 2.6%. Differences among these compositions would consequently have been associated more plausibly with elemental activity, intermetallic formation, diffusion, and corrosion-product chemistry than with configurational entropy alone.

Ti $_3$AlC $_2$ was supported as a sensitive but chemically active sentinel. Its previously reported Al extraction, lamellar degradation, and chlorine penetration in molten LiCl–KCl [2] indicated that chemical resistance drift could have accompanied mechanically induced resistance changes. The protected reference track, dry-Ar $R(T)$calibration, MAX-only controls, and event-triggered microscopy were therefore required for reliable interpretation.

The calculated resistance response further demonstrated that severe localized disruption could have produced a large electrical response. When 50% of the original conducting area remained, $R/R_0 = 2$was obtained. When only 10% remained, $R/R_0 = 10$was obtained. Such nonlinear amplification provided a physical basis for using a very small embedded conducting volume as a damage-sensitive element.

The overall sensing concept could be considered successful only when protection and early warning were demonstrated simultaneously. Rapid electrical response caused by rapid failure of a poorly protective coating would not have represented desirable multifunctional behaviour. Conversely, excellent corrosion resistance without a reproducible depth-specific electrical response would have represented a protective nanolaminate rather than a validated self-sensing coating.

The strongest evidentiary sequence therefore consisted of preservation of useful barrier performance relative to the bare substrate and monolithic HEA, followed by an irreversible temperature-corrected electrical event at a known sensing depth, independent microstructural or chemical confirmation of degradation at the same depth, subsequent electrochemical or salt-chemistry evidence of advanced penetration, and finally a positive value of $\Delta t_{warning}$determined from independent timestamps.

The principal electrical-response classes and the physical evidence required for their interpretation are summarized in Table 7.

Table 7::Evidence required for mechanistic interpretation of the principal electrical-response classes.

Electrical behaviour	Most plausible interpretation	Independent evidence required
Reversible $R(T)$variation	Normal temperature dependence	Dry-Ar calibration and protected reference track
Slow irreversible resistance drift	MAX chemical ageing, Al depletion, Cl incorporation, or phase transformation	XPS, TEM/STEM–EDS/EELS, and Cl/Al depth profiling
Short resistance burst with recovery	Contact disturbance, microcrack opening/closure, or thermal transient	Dummy leads, synchronized temperature, and repeatability
Persistent resistance step	Crack intersection, localized delamination, or partial conducting-section loss	FIB–SEM/TEM at the event location
Near-open-circuit response	Severe track interruption or extensive MAX degradation	Cross-sectional confirmation and continuity testing
Sequential S1→S2→S3 events	Progressive through-thickness penetration	Event-triggered microscopy at corresponding sensing depths
Sensor event followed by substrate-ion release	Potential early warning of breakthrough	ICP blank correction and substrate-specific elemental markers
Resistance event accompanied by major EIS deterioration	Coupled local and global loss of barrier integrity	Synchronized EIS and destructive validation

Electrical resistance was therefore treated as a time-resolved damage observable rather than as a replacement for conventional corrosion characterization. Its mechanistic significance depended on agreement with electrochemical behaviour, dissolved-metal chemistry, and spatially resolved microscopy.

CONCLUSION

The AlCrFeNiSi/Ti_3AlC_2 nanolaminate framework was developed to integrate high-temperature molten-chloride protection with electrically addressable, depth-resolved damage detection. The methodology combined controlled

HEA chemistry, modulation-period engineering, isolated MAX-phase sentinel tracks, four-terminal resistance measurement, specimen-specific thermal correction, electrochemical impedance spectroscopy, dissolved-metal quantification, and event-triggered microstructural characterization. The coating design incorporated a 0.20 µm graded HEA base, a 3.00 µm multilayer region, and a 0.30 µm HEA cap, with 2.50 µm of HEA distributed throughout the multilayer. The Ti_3AlC_2 fraction within the multilayer was calculated as 16.67%, permitting architecture-dependent effects to be separated from changes in phase quantity. Mixing entropies ranged from 12.58 to 12.91 J mol^{-1} K^{-1}, while calculated valence-electron concentrations ranged from 6.43 to 6.75, supporting a BCC/B2-centred compositional strategy without assigning unsupported phase fractions. A 100 µW power ceiling corresponded to approximately 400 Ω at a sensing current of 500 µA, confirming that current selection required track-specific resistance control. The principal experimental matrix contained 56 specimens distributed across protective architectures, sensing configurations, defect controls, and reference materials. A 500 h monitoring sequence generated 92 routine impedance spectra and 30,000 one-minute resistance aggregates, demonstrating the need to distinguish acquisition density from statistical independence. These outcomes establish a rigorous basis for innovative coating selection, sensor calibration, and mechanistically validated early warning. Future investigations will quantify warning intervals using independent failure endpoints, verify nanoscale MAX continuity after thermal processing, assess batch-dependent interdiffusion, and examine durability under impurity variation and thermal cycling. Extended research will also evaluate complex component geometries, alternative MAX phases, and independently deposited batches to determine scalability and predictive transferability in molten-salt energy and reactor systems.

REFERENCES

Ai, H., Chen, Y., Yang, X., Sun, H., Su, X., Yan, L., Huang, W., & Gong, Y. (2024). Intergranular corrosion of 316H stainless steel induced by SO_4^{2-} ions in $MgCl_2$–KCl–NaCl molten salt. Solar Energy Materials and Solar Cells, 271, 112851. doi:10.1016/j.solmat.2024.112851.

Azina, C., Badie, S., Litnovsky, A., Silvestroni, L., Sani, E., & Gonzalez-Julian, J. (2023). Optical properties and corrosion resistance of Ti_2AlC, Ti_3AlC_2, and Cr_2AlC as candidates for concentrated solar power receivers. Solar Energy Materials and Solar Cells, 259, 112433. doi:10.1016/j.solmat.2023.112433.

Choi, S. J., Kim, H. I., Bae, J., Noh, S., & Youn, Y.-S. (2024). Corrosion behavior of alloys 600, 617, and Hastelloy N in molten KCl salt. Solar Energy Materials and Solar Cells, 275, 113026. doi:10.1016/j.solmat.2024.113026.

Ding, W., Yang, F., Bonk, A., & Bauer, T. (2021). Molten chloride salts for high-temperature thermal energy storage: Continuous electrolytic salt purification with two Mg-electrodes and alternating voltage for corrosion control. Solar Energy Materials and Solar Cells, 223, 110979. doi:10.1016/j.solmat.2021.110979.

Dong, D., Liu, G., Guo, W., Zhang, Y., Ding, N., Liu, L., Xu, N., Chen, L., An, Y., & Bai, Y. (2025). The effect of heat-treatment on microstructure, wear resistance, and corrosion resistance of laser cladding $AlCoCrFeNi_{2.1}$ high entropy alloy coating. Intermetallics, 180, 108693. doi:10.1016/j.intermet.2025.108693.

Gong, Q., Shi, H., Chai, Y., Yu, R., Weisenburger, A., Wang, D., Bonk, A., Bauer, T., & Ding, W. (2022). Molten chloride salt technology for next-generation CSP plants: Compatibility of Fe-based alloys with purified molten $MgCl_2$–KCl–NaCl salt at 700 °C. Applied Energy, 324, 119708. doi:10.1016/j.apenergy.2022.119708.

Gong, Q., Hanke, A., Kessel, F., Bonk, A., Bauer, T., & Ding, W. (2023). Molten chloride salt technology for next-generation CSP plants: Selection of cold tank structural material utilizing corrosion control at 500 °C. Solar Energy Materials and Solar Cells, 253, 112233. doi:10.1016/j.solmat.2023.112233.

Grégoire, B., Oskay, C., Meißner, T. M., & Galetz, M. C. (2020). Corrosion mechanisms of ferritic-martensitic P91 steel and Inconel 600 nickel-based alloy in molten chlorides. Part II: NaCl–KCl–$MgCl_2$ ternary system. Solar Energy Materials and Solar Cells, 216, 110675. doi:10.1016/j.solmat.2020.110675.

Li, H., Cao, H., Liu, F., Li, Y., Qi, F., Ouyang, X., & Zhao, N. (2022). Microstructure, mechanical and electrochemical properties of Ti_3AlC_2 coatings prepared by filtered cathode vacuum arc technology. Journal of the European Ceramic Society, 42(5), 2073–2083. doi:10.1016/j.jeurceramsoc.2021.12.066.

Li, X., Xu, T., Liu, M., Song, Y., Zuo, Y., Tang, Z., Yan, L., & Wang, J. (2022). Thermodynamic and kinetic corrosion behavior of alloys in molten $MgCl_2$–NaCl eutectic: FPMD simulations and electrochemical technologies. Solar Energy Materials and Solar Cells, 238, 111624. doi:10.1016/j.solmat.2022.111624.

Li, Z., Zhou, G., Wang, Z., Yuan, J., Ke, P., & Wang, A. (2023). HiPIMS induced high-purity Ti_3AlC_2 MAX phase coating at low-temperature of 700 °C. Journal of the European Ceramic Society, 43(11), 4673–4683. doi:10.1016/j.jeurceramsoc.2023.03.059.

Liu, T., Zhang, D., Ma, L., Huang, Y., Hao, X., Terryn, H., Mol, A., & Li, X. (2022). Smart protective coatings with self-sensing and active corrosion protection dual functionality from pH-sensitive calcium carbonate microcontainers. Corrosion Science, 200, 110254. doi:10.1016/j.corsci.2022.110254.

Magnus, C., Cooper, D. J., Jantzen, C., Lambert, H., Abram, T. J., & Rainforth, M. (2021). Synthesis and high temperature corrosion behaviour of nearly monolithic Ti_3AlC_2 MAX phase in molten chloride salt. Corrosion Science, 182, 109193. doi:10.1016/j.corsci.2020.109193.

Odabas, O., Karaoglanli, A. C., & Ozgurluk, Y. (2024). Microstructural evolution and high temperature hot corrosion behaviour of AlCoCrFeNiTi high-entropy alloy coatings. Materials Today Communications, 41, 110910. doi:10.1016/j.mtcomm.2024.110910.

Patel, K., Sadeghilaridjani, M., Pole, M., & Mukherjee, S. (2021). Hot corrosion behavior of refractory high entropy alloys in molten chloride salt for concentrating solar power systems. Solar Energy Materials and Solar Cells, 230, 111222. doi:10.1016/j.solmat.2021.111222.

Patel, K., Mahajan, C., Muskeri, S., & Mukherjee, S. (2023a). Corrosion behavior of refractory high-entropy alloys in FLiNaK molten salts. Metals, 13(3), 450. doi:10.3390/met13030450.

Patel, K., Hasannaeimi, V., Sadeghilaridjani, M., Muskeri, S., Mahajan, C., & Mukherjee, S. (2023b). Molten salt corrosion behavior of dual-phase high entropy alloy for concentrating solar power systems. Entropy, 25(2), 296. doi:10.3390/e25020296.

Shi, H., Azmi, R., Han, L., Tang, C., Weisenburger, A., Heinzel, A., Maibach, J., Stüber, M., Wang, K., & Müller, G. (2022). Corrosion behavior of Al-containing MAX-phase coatings exposed to oxygen containing molten Pb at 600 °C. Corrosion Science, 201, 110275. doi:10.1016/j.corsci.2022.110275.

Takeyama, M. (2025). High-temporal-resolution corrosion monitoring in fluctuating-temperature environments with an improved electrical resistance sensor. Sensors, 25(1), 268. doi:10.3390/s25010268.

Villada, C., Ding, W., Bonk, A., & Bauer, T. (2021). Engineering molten $MgCl_2$–KCl–NaCl salt for high-temperature thermal energy storage: Review on salt properties and corrosion control strategies. Solar Energy Materials and Solar Cells, 232, 111344. doi:10.1016/j.solmat.2021.111344.

Wang, C., Ma, X., Zhang, H., Zhang, Y., Wang, F., & Song, B. (2022). Chloride corrosion property evolution of CrMnFeCoNi high-entropy alloy coating. Materials Science and Technology, 38(16), 1418–1424. doi:10.1080/02670836.2022.2080388.

Wu, H., Xie, J., Yang, H., Sheng, N., Yang, Y., Hou, G., Li, J., Zhou, Y., & Sun, X. (2023). Corrosion behaviors and passive film properties of a newly developed cost-effective AlCrFeNi eutectic high entropy alloy in different corrosive solutions. Materials Today Communications, 37, 107602. doi:10.1016/j.mtcomm.2023.107602.

Xiao, H., Wang, Y., Gu, L., Feng, Z., Lei, B., Zhu, L., Guo, H., & Meng, G. (2023). Smart sensing coatings for early warning of degradations: A review. Progress in Organic Coatings, 177, 107418. doi:10.1016/j.porgcoat.2023.107418.

Xie, Z., Liu, B., Fu, A., Li, K., Cao, Y., Zhou, H., Peng, J., & Liu, Y. (2024). Combating Cl^- and SO_4^{2-}-induced molten salt corrosion by laser cladding FeCrNiMoAl high-entropy alloy coating. Surface and Coatings Technology, 494, 131429. doi:10.1016/j.surfcoat.2024.131429.

Yang, K., Lei, Y., Tong, B., & Zhang, S. (2025). Composition-driven microstructure evolution of $AlCrCu_{1-x}Mo_xNi$ high-entropy alloy coatings: Understanding composite molten salt corrosion mechanisms at 700 °C. Materials Characterization, 230, 115745. doi:10.1016/j.matchar.2025.115745.

Yuan, S., Li, H., Han, C., Li, W., Xu, X., Chen, C., Wei, R., Wang, T., Wu, S., & Li, F. (2023). FeCoNiCrAl$_{0.6}$ high-entropy alloy coating on Q235 steel fabricated by laser cladding. Materials Science and Technology, 39(6), 705–713. doi:10.1080/02670836.2022.2132734.

Zhang, L., Ji, Y., & Yang, B. (2023). Thermal stability and hot corrosion performance of the AlCoCrFeNi$_{2.1}$ high-entropy alloy coating by laser cladding. Materials, 16(17), 5747. doi:10.3390/ma16175747.

Zhang, L., Ji, Y., Wang, Y., & Yang, B. (2024). Enhanced hot corrosion resistance of AlCoCrFeNi$_{2.1}$ high entropy alloy coatings by extreme high-speed laser cladding. Corrosion Science, 240, 112486. doi:10.1016/j.corsci.2024.112486.

Zhao, Q., Pan, Z., Wang, X., Luo, H., Liu, Y., & Li, X. (2022). Corrosion and passive behavior of Al$_x$CrFeNi$_{3-x}$ (x = 0.6, 0.8, 1.0) eutectic high entropy alloys in chloride environment. Corrosion Science, 208, 110666. doi:10.1016/j.corsci.2022.110666.

Zhao, Y., & Gomez-Vidal, J. C. (2020). Potential scalability of a cost-effective purification method for MgCl$_2$-containing salts for next-generation concentrating solar power technologies. Solar Energy Materials and Solar Cells, 215, 110663. doi:10.1016/j.solmat.2020.110663.

Boschen, M., Meghwal, A., Bosi, E., Hong, S.-J., Berndt, C. C., Ang, A. S. M., et al. Oxidation behaviour of an AlCrFeNiSi-based high-entropy alloy bond coat designed with the CALPHAD approach. npj Materials Degradation **10** (2026) 64. https://doi.org/10.1038/s41529-026-00778-9.

Magnus, C., Cooper, D., Jantzen, C., Lambert, H., Abram, T., Rainforth, M. Synthesis and high temperature corrosion behaviour of nearly monolithic Ti $_3$AlC $_2$ MAX phase in molten chloride salt. Corrosion Science **182** (2021) 109193. https://doi.org/10.1016/j.corsci.2020.109193.

Li, Z., Zhou, G., Wang, Z., Yuan, J., et al. HiPIMS-induced high-purity Ti $_3$AlC $_2$ MAX-phase coating at low temperature. Journal of the European Ceramic Society **43** (2023) 4673–4683. https://doi.org/10.1016/j.jeurceramsoc.2023.03.059.

Gong, Q., Shi, H., Chai, Y., Yu, R., Weisenburger, A., Wang, D., Bonk, A., Bauer, T., Ding, W. Molten chloride salt technology for next-generation CSP plants: Compatibility of Fe-based alloys with purified molten MgCl $_2$–KCl–NaCl salt at 700 °C. Applied Energy **324** (2022) 119708. https://doi.org/10.1016/j.apenergy.2022.119708.

Zhao, Y., Vidal, J. Potential scalability of a cost-effective purification method for MgCl $_2$-containing salts for next-generation concentrating solar power technologies. Solar Energy Materials and Solar Cells **215** (2020) 110663. https://doi.org/10.1016/j.solmat.2020.110663.

Choi, S., Steppan, J. J., Simpson, M. F., et al. Long-term stability of mullite- and magnesia-encased Ag|Ag $^+$ reference electrodes in molten MgCl $_2$–KCl–NaCl. Journal of The Electrochemical Society **170** (2023) 057505. https://doi.org/10.1149/1945-7111/acd35a.